(12) INTERNATIONAL APPLICATION PUBLISHED UNDER THE PATENT COOPERATION TREATY (PCT)

(19) World Intellectual Property Organization
International Bureau

(43) International Publication Date
25 July 2013 (25.07.2013)

WIPO | PCT

(10) International Publication Number
WO 2013/109446 A1

(51) International Patent Classification:
H01L 21/20 (2006.01)

(21) International Application Number:
PCT/US2013/020841

(22) International Filing Date:
9 January 2013 (09.01.2013)

(25) Filing Language: English

(26) Publication Language: English

(30) Priority Data:
61/588,110 18 January 2012 (18.01.2012) US

(71) Applicant: **THE TRUSTEES OF COLUMBIA UNIVERSITY IN THE CITY OF NEW YORK** [US/US]; 412 Low Memorial Library, 535 West 116th Street, New York, NY 10027 (US).

(72) Inventors; and
(71) Applicants *(for US only)*: **GU, Tingyi** [CN/CN]; 171-Wen-er Road, Shi Yuan Xin Cun, Apt. 207, Hangzhou, Zhejiang, 310012 (CN). **WONG, Chee, Wei** [SG/SG]; 36 Toh Tuck Walk, Singapore 596615 (SG).

(74) Agent: **CHIARINI, Lisa, A.**; Hughes Hubbard & Reed LLP, One Battery Park Plaza, New York, NY 10004 (US).

(81) Designated States *(unless otherwise indicated, for every kind of national protection available)*: AE, AG, AL, AM, AO, AT, AU, AZ, BA, BB, BG, BH, BN, BR, BW, BY, BZ, CA, CH, CL, CN, CO, CR, CU, CZ, DE, DK, DM,

[Continued on next page]

(54) Title: OPTOELECTRONIC DEVICES AND METHODS OF FABRICATING SAME

(57) Abstract: A hybrid graphene - silicon optical cavity for chip-scale optoelectronics having attributes including resonant optical bistability for photonic logic gates and memories at femtojoule level switching per bit, temporal regenerative oscillations for self-pulsation generation at record femtojoule cavity circulating powers, and graphene-cavity enhanced four-wave mixing at femtojoule energies on the chip.

Figure 1A

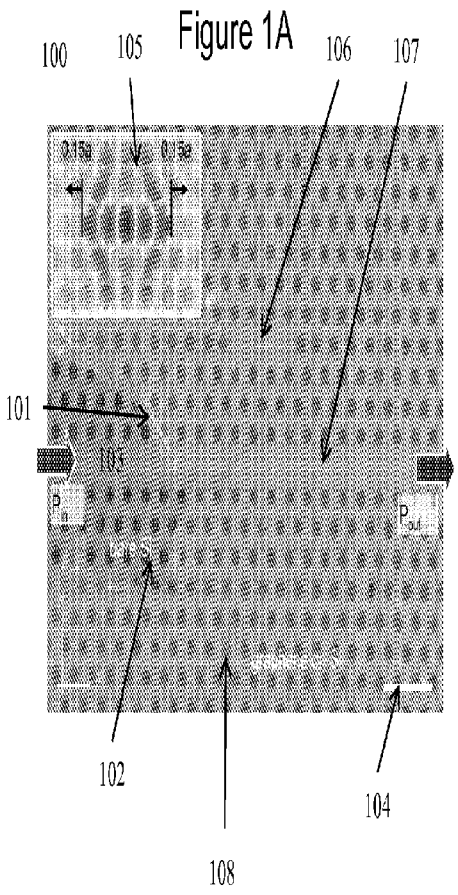

WO 2013/109446 A1

DO, DZ, EC, EE, EG, ES, FI, GB, GD, GE, GH, GM, GT, HN, HR, HU, ID, IL, IN, IS, JP, KE, KG, KM, KN, KP, KR, KZ, LA, LC, LK, LR, LS, LT, LU, LY, MA, MD, ME, MG, MK, MN, MW, MX, MY, MZ, NA, NG, NI, NO, NZ, OM, PA, PE, PG, PH, PL, PT, QA, RO, RS, RU, RW, SC, SD, SE, SG, SK, SL, SM, ST, SV, SY, TH, TJ, TM, TN, TR, TT, TZ, UA, UG, US, UZ, VC, VN, ZA, ZM, ZW.

(84) Designated States *(unless otherwise indicated, for every kind of regional protection available)*: ARIPO (BW, GH, GM, KE, LR, LS, MW, MZ, NA, RW, SD, SL, SZ, TZ, UG, ZM, ZW), Eurasian (AM, AZ, BY, KG, KZ, RU, TJ, TM), European (AL, AT, BE, BG, CH, CY, CZ, DE, DK, EE, ES, FI, FR, GB, GR, HR, HU, IE, IS, IT, LT, LU, LV, MC, MK, MT, NL, NO, PL, PT, RO, RS, SE, SI, SK, SM, TR), OAPI (BF, BJ, CF, CG, CI, CM, GA, GN, GQ, GW, ML, MR, NE, SN, TD, TG).

Published:

— *with international search report (Art. 21(3))*

OPTOELECTRONIC DEVICES AND METHODS OF FABRICATING SAME

PRIORITY CLAIM

[0001] This application claims priority to United States Provisional Application Serial No. 61/588,110, filed January 18, 2012, the entire contents of which is hereby incorporated by reference.

STATEMENT REGARDING FEDERALLY SPONSORED RESEARCH

[0002] This invention was made with government support under grant number DGE1069240 awarded by the National Science Foundation and grant number DE-SC0001085 awarded by the U.S. Department of Energy. The government has certain rights in the invention.

FIELD

[0003] The embodiments of the disclosed subject matter relate to optoelectronic devices. More particularly, the embodiments of the subject matter relate to graphene-clad photonic crystals and methods of fabrication thereof.

BACKGROUND

[0004] The unique linear and massless band structure of graphene, in a purely two-dimensional Dirac fermionic structure, has led to intense research spanning from condensed matter physics to nanoscale device applications covering the electrical, thermal, mechanical and optical domains.

[0005] Sub-wavelength nanostructures in monolithic material platforms have witnessed rapid advances towards chip-scale optoelectronic modulators, photoreceivers, and high-bitrate signal processing architectures. Coupled with ultrafast nonlinearities as a new parameter space for optical physics, breakthroughs such as resonant four-wave mixing and parametric femtosecond pulse characterization have been described. Recently, graphene – with its broadband dispersionless nature and large carrier mobility – has been examined for its gate-variable optical transitions towards broadband ultrafast electroabsorption modulators and photoreceivers, as well as saturable absorption for mode-locking. Due to its linear band structure allowing interband optical transitions at all photon energies, graphene has been suggested as a material with large $\chi^{(3)}$ nonlinearities.

[0006] There remains a need for a photonic crystal with improved optical characteristics and higher energy efficiency. In particular, low-power bistability, regenerative oscillation, a high Kerr coefficient, and efficient four-wave mixing are desirable in optical telecommunications and other optical signal processing applications.

SUMMARY

[0007] In one aspect of the disclosed subject matter a photonic crystal is provided. In one embodiment, the photonic crystal comprises a body having opposing top and bottom surfaces and formed from at least a silicon material. The top and bottom surfaces can be substantially parallel to each other. The body includes a plurality of cavities defining a plurality of openings extending at least partially through the opposing top and bottom surfaces. At least some of the cavities can define an opening through both the top and bottom surfaces of the crystal body. Graphene is disposed on at least the top surface of the body. In some embodiments, only a monolayer is disposed on the crystal body. The monolayer can be substantially optically transparent to infrared.

[0008] The defined openings can be substantially cylindrical in shape. Each of the plurality of cavities can define an opening having a radius between about 122nm and about 126nm. The plurality of cavities can be arranged in a variety of patterns. For example, the cavities can define a hexagonal pattern. The pattern can comprise one or more discontinuity. A lattice constant of the plurality of cavities can be about 420 nm. The distance between the opposing top and bottom surfaces can be about 250 nm.

[0009] The graphene-clad photonic crystal described and embodied herein can exhibit (1) ultralow power resonant optical bistability; (2) self-induced regenerative oscillations; and (3) ultrafast coherent four-wave mixing, all at a few femtojoule cavity recirculating energies. Without being held to any theory, these attributes are believed to be due to the dramatically-large and ultrafast $\chi^{(3)}$ nonlinearities in graphene and the large Q/V ratios in wavelength-localized photonic crystal cavities. The hybrid two-dimensional graphene-silicon nanophotonic devices according to one aspect of the present disclosure are particularly well-suited for next-generation chip-scale ultrafast optical communications, radio-frequency optoelectronics, and all-optical signal processing.

[0010] In yet another aspect, a method of fabricating a photonic crystal is provided. The method comprises providing a foil, removing a top layer of the foil, depositing carbon on the foil to form a graphene layer, coating the graphene layer with a polymer, removing the graphene layer from the foil, and transferring the graphene layer onto a silicon body, and removing the polymer coating. The method can further comprise defining a plurality of cavities in the silicon body by various techniques known in the art. One example is by deep-ultraviolet lithography.

[0011] It is to be understood that both the foregoing general description and the following detailed description are exemplary and are intended to provide further explanation of the disclosed subject matter claimed.

BRIEF DESCRIPTION OF THE FIGURES

[0012] **Figures 1A-1D** depict graphene-cladded silicon photonic crystal nanostructures according to an embodiment of the present subject matter.

[0013] **Figures 2A-2B** depict bistable switching in graphene-cladded nanocavities according to an embodiment of the present subject matter.

[0014] **Figures 3A-3D** depict regenerative oscillations in graphene-cladded nanocavities according to an embodiment of the present subject matter.

[0015] **Figures 4A-4D** depict parametric four-wave mixing in graphene-cladded silicon nanocavities according to an embodiment of the present subject matter.

[0016] **Figures 5A-5D** depict Raman spectrum and transferred graphene samples according to an embodiment of the present subject matter.

[0017] **Figure 6** depicts a comparison of switching energy versus recovery time of cavity-based modulators and switches across different semiconductor material platforms.

[0018] **Figures 7A-7D** depict steady-state two-photon absorption induced thermal nonlinearities in graphene-silicon hybrid cavities according to an embodiment of the present subject matter.

[0019] **Figure 8A-8B** depict coupled-mode equations calculated self-induced optical regenerative oscillations with a silicon photonic crystal *L3* nanocavity side-coupled to a photonic crystal waveguide according to an embodiment of the present subject matter.

[0020] **[0001]Figure 9** depicts free-carrier absorption effects on the four-wave mixing conversion efficiency according to an embodiment of the present subject matter.

DETAILED DESCRIPTION OF EXEMPLARY EMBODIMENTS

[0021] Generally, the disclosed subject matter provides a graphene-clad photonic crystal that exhibits beneficial optical properties, and a method of fabrication thereof. The graphene-clad photonic crystal can provide ultralow power optical bistable switching, self-induced regenerative oscillations, and ultrafast coherent four-wave mixing at femtojoule cavity energies on the semiconductor chip platform. Thus the disclosed subject matter is particularly well-suited for various applications including next-generation chip-scale ultrafast optical communications, radio-frequency optoelectronics and optical signal processing.

[0022] In one embodiment, as shown in **Figure 1A**, the photonic crystal **100** comprises a body **102** having opposing top and bottom surfaces, the body formed from at least a silicon material. The top and bottom surfaces of body 102 can be parallel or substantially parallel to each other. The body includes a plurality of cavities **108** defining a plurality of openings extending at least partially through the opposing top and/or bottom surfaces. At least some of the cavities **108** can define an opening through both the top and bottom surfaces of the crystal body **102**, and in some embodiments each of the plurality of cavities define an opening through both top and bottom surfaces. Graphene **101** is disposed on at least the top surface of the body 102. Accordingly, the structure according to this embodiment can include hybrid graphene-silicon cavitities that can be achieved by rigorous transfer of a monolayer large-area graphene sheet onto an air-bridged silicon photonic crystal nanomembrane with minimal linear absorption and optimized optical input/output coupling. This structure can be complemented with large-area graphene field-effect transistors and analog circuit designs for potential large-scale silicon integration.

[0023] The graphene-cladded photonic crystal nanomembranes **100** can include an optical nanocavity **106**; a point-defect photonic crystal *L3* cavity (with three missing holes), with nearest holes at the cavity edges tuned by $0.15a$ where a is the photonic crystal lattice

constant. Lattice constant *a* can be for example 420 nm. The *L3* cavity is side coupled to a photonic crystal line defect waveguide **107** for optical transmission measurements. In some embodiments, chemical vapor deposition (CVD) grown graphene can be wet-transferred onto the silicon nanomembrane with the graphene heavily *p*-doped, on a large sheet without requiring precise alignment.

[0024] As illustrated in **Figure 1A**, the graphene can be a monolayer **101** that covers silicon body **102**. A bare silicon region **103** is depicted showing the graphene monolayer **101** separated from the silicon **102** body and is provided only for illustration purposes. A scale bar **104** of 500 nm is provided for illustration. Inset **105** provides an example *Ez*-field from finite-difference time-domain computations.

[0025] Referring to **Figure 1B** Measured Raman scattering spectra of monolayer CVD-grown graphene on a photonic crystal cavity membrane is shown. The Lorentzian lineshape full-width half-maximum of the *G* band **111** (34.9 cm^{-1}) and *2D* band **112** (49.6 cm^{-1}) peaks and the *G*-to-*2D* peak ratio indicates the graphene monolayer, while the single symmetric *G* peak **111** indicates good graphene uniformity. Homogeneity across the sample is shown by exciting at different locations on the cavity membrane (curves **113**, **114**, and **115**). The single layer graphene **101** is identified by Raman spectroscopy via the full-width half-maximum of the *G* (**111**) and *2D* (**112**) band peaks (34.9 cm^{-1} and 49.6 cm^{-1} respectively) and the *G*-to-*2D* peak intensity ratio of ~ 1 to 1.5. The *G* band lineshape **111** is a single and symmetrical Lorentzian indicating good uniformity graphene. Heavily doped graphene is prepared to achieve optical transparency in the infrared with negligible linear losses, as the Fermi level is below the one-photon interband optical transition threshold (**Figure 1C** inset **125**) and intraband graphene absorption is near-absent in the infrared.

[0026] Referring to **Figure 1C** a SEM **120** of suspended graphene-silicon membrane is provided. Dark patches **121** denote bilayer graphene. The left inset **122** provides a Dirac

cone illustrating the highly-doped Fermi level (dashed circle **123**) allowing only two-photon transition (solid arrows **124**) while the one-photon transition (dashed arrow **125**) is forbidden. The right inset **126** provides a computed *Ey*-field along the *z*-direction, with graphene at the evanescent top interface. The scale bar **127** at lower right is 500 nm.

[0027] **Figure 1D** depicts an example measured graphene-cladded cavity transmission with asymmetric Fano-like lineshapes **131**, compared to a control bare Si cavity sample with symmetric Lorentzian lineshapes **132**. Both spectra are measured at 0.6 mW input power, with similar intrinsic cavity quality factors between the graphene and the control sample. The cavity transmissions are centered to the intrinsic cavity resonances at low power (less than 100 uW input power). Transverse-electric (TE) polarization laser light is launched onto the optical cavity and evanescently coupled to the monolayer graphene. As shown in **Figure 1D**, the cavity transmission spectra, performed with tunable continuous-wave laser sources, shows a consistent and large resonance red-shift of 1.2 nm/mW, approximately 4× larger than that of a near-identical control cavity without graphene.

[0028] The low power "cold cavity" transmissions taken at 2.5 μW input powers depict intrinsic *Q*s of 22,000 and loaded *Q*s of 7,500, with background Fabry-Perot oscillations arising from the input/output facet coupling reflections (~ 0.12 reflectivity). The high power cavity transmission is not only red-shifted to *outside* the cold cavity lineshape full-width base but also exhibit a Fano-like asymmetric lineshape, with good matching to coupled-mode model predictions. With the transferred monolayer graphene onto only the short photonic crystal regions the total fiber-chip-fiber transmission is decreased by less than 1 dB, slightly better than the 5-dB additional loss in modified graphene-fiber linear polarizers (with different cavity or propagation lengths and evanescent core coupling). For the same increased cavity power on a monolithic silicon cavity without graphene, both control

experiments and numerical models show a negligible thermal red-shift of 0.1 nm/mW, for the power levels and the specific loaded cavity Q^2/V values [of $4.3\times10^7(\lambda/n)^3$] described herein.

[0029] Referring to **Figure 2A** steady-state input/output optical bistability for the quasi-TE cavity mode with laser-cavity detuning δ at 1.5 (**201**) and 1.7 (**202**) is depicted. The dashed line **203** is the coupled-mode theory simulation with effective nonlinear parameters of the graphene-silicon cavity sample. The large frequency shifts from the graphene-cladded hybrid photonic cavity exhibit low-threshold optical bistability. **Figure 2A** shows the observed bistability at 100 μW threshold powers for a loaded cavity Q of 7,500, with cavity – input laser detuning δ of 1.5 with δ defined as $(\lambda_{laser} - \lambda_{cavity})/\Delta\lambda_{cavity}$, where $\Delta\lambda_{cavity}$ is the cold cavity full-width half-maximum linewidth. The steady-state bistable hystersis at a detuning of 1.7 is also illustrated in **Figure 2A**. The dashed line **203** shows the coupled-mode theory numerical predictions of the hybrid cavity, including first-order estimates of the graphene-modified thermal, linear and nonlinear loss, and free carrier parameters (detailed below). The heavily-doped graphene has a two-photon absorption at least several times larger than silicon, described by its isotropic bands for interband optical transitions, leading to increased free carrier densities/absorption and overall enhanced thermal red-shift.

[0030] **Figure 2B** depicts switching dynamics with triangular waveform drive input. The bistable resonances are shown for both positive and negative detuning. Empty circles signify δ(t=0)=-1.3 (211), while solid circles signify δ(t=0) =1.6 (212). The inset (213) contains a schematic of high-and low-state transmissions. Bistable switching dynamics can be verified by inputting time-varying laser intensities to the graphene-cladded cavity, allowing a combined cavity power – detuning sweep. Thus, **Figure 2B** shows an example time-domain output transmission for two different initial detunings [$\delta_{(t=0)}$= -1.3 (**211**) and $\delta_{(t=0)}$=1.6 (**212**)] and for an illustrative triangular-waveform drive, with nanosecond resolution on an amplified photoreceiver. With the drive period at 77 ns, the observed thermal

relaxation time is ~ 20 ns. Cavity resonance dips (with modulation depths ~ 3-dB in this example) are observed for both positive detuning (up to 0.07 nm, δ = 0.58) and negative detuning (in the range from -0.15 nm (δ = 0.75) to -0.10 nm (δ = 0.5).

[0031] The respective bistable high- and low-state transmissions are illustrated in the inset **213** of **Figure 2B**, for each bistability switching cycle. Bistability with both detunings are observable – with the negative detuning, the carrier-induced (Drude) blue-shifted dispersion overshoots the cavity resonance from the drive frequency and then thermally pins the cavity resonance to the laser drive frequency (see below). Since the free carrier lifetime of the hybrid media is about 200 ps and significantly lower than the drive pulse duration, these series of measurements are thermally dominated; the clear (attenuated) resonance dips on the intensity up-sweeps (down-sweeps) are due to the measurement sampling time shorter than the thermal relaxation timescale and a cooler (hotter) initial cavity temperature.

[0032] When the input laser intensity is well above the bistability threshold, the graphene-cavity system deviates from the two-state bistable switching and becomes oscillatory as shown in **Figure 3A**. **Figure 3A** depicts observations of temporal regenerative oscillations in the cavity for optimized detuning (0.11 nm). The input power is quasi-triangular waveform with peak power 1.2 mW. The grey line **301** is the reference output power, with the laser detuning 1.2 nm from cavity resonance. Regenerative oscillation is theoretically predicted in GaAs nanocavities with large Kerr nonlinearities or observed in high-Q (3×10^5) silicon microdisks. These regenerative oscillations are formed between the competing phonon and free carrier populations, with slow thermal red-shifts (~ 10 ns timescales) and fast free-carrier plasma dispersion blue-shifts (~ 200 ps timescales) in the case of a graphene-silicon cavity resonance according to an embodiment of the present subject matter. The self-induced oscillations across the drive laser frequency are observed at threshold cavity powers of 0.4 mW, at ~ 9.4 ns periods in these series of measurements

which gives ~ 106 MHz modulation rates, at experimentally-optimized detunings from $\delta_{(t=0)}$ = 0.68 to 1.12. For a monolithic silicon *L3* cavity, such regenerative pulsation has not been previously observed nor predicted to be observable at a relatively modest Q of 7,500 (see below). The temporal coupled-mode models for a conventional silicon photonic crystal cavity predict the threshold for regenerative oscillations to be at least 20 mW (even higher than the tunable laser output discussed herein), with significant nonlinear absorption.

[0033] **Figure 3B** maps the output power versus input power with slow up (crosses **311**) and down (dots **312**) power sweeping. In the up-sweep process, the cavity starts to oscillate when the input power is beyond 0.2 mW, but the oscillation is not observed in the down-sweep process. The input-output intensity loop constructed from the temporal response measurements of a triangular-wave modulated 1.2 mW laser with a 2 μs cycle is shown. Clear bistability behavior is seen below the carrier oscillation threshold. The system transits to the regime of self-sustained oscillations as the power coupled into the cavity is above the threshold, by tuning the laser wavelength into cavity resonance.

[0034] **Figure 3C** depicts nonlinear coupled-mode theory model of cavity transmission versus resonance shift, in the regime of regenerative oscillations. With a detuning of 0.15 nm [δ(t=0)=0.78] the free carrier density swings from 4.4 to 9.1×10^{17} per cm^3 and the increased temperature circulates between 6.6 and 9.1K. The fast free-carrier response fires the excitation pulse (dashed line **321** in **Figure 3C**), and the heat diffusion determines the recovery to the quiescent state. In the graphene-cladded suspended silicon membrane, the heat diffusion time constant is slow enough for the cavity to catch up with the free carrier dispersion. **Figure 3D** depicts the spectrum of cavity energy at below (0.2 mW, dashed line **331**) and beyond oscillation threshold (0.6 mW, solid line **332**) at the same detuning δ(t=0)=0.78, as in **Figure 3C**. Inset **333** depicts normalized transmission from model (line **334**) and experimental data at the same constant power level (circles **335**). The beating rate

between the thermal and free carrier population is around 50 MHz, as shown in inset **333** of **Figure 3D**, with the matched experimental data and coupled-mode theory simulation. The beating gives rise to peaks in the radio-frequency frequency spectra (Figure 3D; solid line **332**), which are absent when the input power is below the oscillation threshold (dashed line **331**).

[0035] To examine only the Kerr nonlinearity, degenerate four-wave mixing measurements can be performed on the hybrid graphene – silicon photonic crystal cavities as illustrated in **Figure 4**, with continuous-wave laser input. **Figure 4A** depicts measured transmission spectrum with signal laser fixed at -0.16 nm according to cavity resonance, and pump laser detuning is scanned from -0.1 to 0.04 nm. The inset **401** provides a band diagram of degenerate four-wave mixing process with pump (**402**), signal (**403**) and idler (**404**) lasers. **Figure 4B** depicts measured transmission spectrum with pump laser fixed on cavity resonance, and signal laser detuning is scanned from -0.05 to -0.25 nm.

[0036] A lower-bound Q of 7,500 was chosen to allow a ~ 200 pm cavity linewidth within which the highly dispersive four-wave mixing can be examined. The input pump and signal laser detunings are placed within this linewidth, with matched TE-like input polarization, and the powers set at 600 μW. Two example series of idler measurements are illustrated in **Figure 4A** and **4B**, with differential pump and signal detunings respectively. In both series the parametric idler is clearly observed as a sideband to the cavity resonance, with the pump detuning ranging -100 pm to 30 pm and the signal detuning ranging from -275 pm to -40 pm, and from 70 pm to 120 pm. For each fixed signal- and pump-cavity detunings, the generated idler shows a slight intensity roll-off from linear signal (or pump) power dependence when the transmitted signal (or pump) power is greater than ~ 400 μW due to increasing free-carrier absorption effects (**Figure 9** described below). As illustrated in **Figure 4A** and **4B**, the converted idler wave shows a four-wave mixing 3-dB bandwidth

roughly matching the cavity linewidth when the pump laser is centered at the cavity resonance.

[0037] **[0002]**A theoretical four-wave mixing model with cavity field enhancement (**Figure 4C** and **4D**) matches with these first graphene-cavity observations, and is described in further detail below. **Figure 4C** depicts modeled conversion efficiency versus pump and signal detuning from the cavity resonance. The solid lines **421** and dashed lines **422** mark the region plotted in **Figures 4A** and **4B** respectively. **Figure 4D** depicts observed and simulated conversion efficiency of the cavity. Solid dots **431** are measured with signal detuning as in **Figure 4B**, and the empty circles **432** are obtained through pump detuning as in **Figure 4A**, plus 29.5-dB (off set due to the 0.16 nm signal detuning). Solid line **433** and dashed line **434** are modeled conversion efficiencies of graphene-silicon and monolithic silicon cavities respectively. Grey dashed line **435** (superimposed) provides an illustrative pump/signal laser spontaneous emission noise ratio.

[0038] Based on the numerical model match to the experimental observations, the observed Kerr coefficient n_2 of the graphene-silicon cavity ensemble is 4.8×10^{-17} m^2/W, an order of magnitude larger than in monolithic silicon and GaInP-related materials, and two orders of magnitude larger than in silicon nitride. Independently, the field-averaged effective $\chi^{(3)}$ and n_2 of the hybrid graphene-silicon cavity can also be modeled as described in equation (1), where $E(r)$ is the complex fields in the cavity, $n(r)$ is local refractive index, λ_0 is the wavelength in vacuum, and d is the number of dimensions (3).

$$\overline{n_2} = \left(\frac{\lambda_0}{2\pi}\right)^d \frac{\int n^2(r) n_2(r)\left(|E(r)\cdot E(r)|^2 + 2|E(r)\cdot E(r)^*|^2\right) d^d r}{\left(\int n^2(r)|E(r)|^2 d^d r\right)^2} \qquad (1)$$

[0039] As detailed below, the computed n_2 is at 7.7×10^{-17} m^2/W, matching well with the observed four-wave mixing derived n_2. The remaining discrepancies arise from a Fermi velocity slightly smaller than the ideal values ($\sim 10^6$ m/s) in the graphene. As illustrated in

Figure 4D for both measurement and theory, the derived conversion efficiencies are observed up to -30-dB in the unoptimized graphene-cavity, even at cavity *Q*s of 7,500 and low pump powers of 600 μW. The highly-doped graphene with Fermi-level level in the optical transparency region is a pre-requisite to these observations. For a monolithic silicon cavity the conversion efficiencies are dramatically lower (by more than 20-dB) as shown in dashed black line **434**, and even below the pump/signal laser spontaneous emission noise ratio (dotted grey line **435**) preventing four-wave mixing observation in a single monolithic silicon photonic crystal cavity till now.

Methods of Device Fabrication

[0040] Generally, the method of device fabrication comprises the steps of providing a foil, removing a top layer of the foil, depositing carbon on the foil to form a graphene layer, coating the graphene layer with a polymer, removing the graphene layer from the foil, and transferring the graphene layer onto a silicon body, and removing the polymer coating. The method further comprises defining a plurality of cavities in the silicon body by various techniques known in the art.

[0041] In one embodiment, the photonic crystal can be defined by 248 nm deep-ultraviolet lithography in the silicon CMOS foundry onto an undoped silicon-on-insulator body. Optimized lithography and reactive ion etching can be used to produce device lattice constants of 420 nm, hole radius of 124 ± 2 nm. The photonic crystal cavities and waveguides can be designed and fabricated on a silicon body having 250 nm thickness, followed by a buffered hydrofluoric wet-etch of the 1 um buried oxide to achieve the suspended photonic crystal nanomembranes.

[0042] For example, centimeter-scale graphene can be grown on 25 um thick copper foils by chemical vapor deposition of carbon. The top oxide layer of copper can be removed in

the hydrogen atmosphere (50 mTorr, 2 sccm H_2, 1000°C 15 min), then monolayer carbon can be formed on the copper surface (250 mTorr, 1000 °C, 35 sccm CH_4, 2 sccm H_2 for 30 min). The growth is self-limited once the carbon atom covers the Cu surface catalytic. Then single layer graphene can be fast cooled down. Poly-methyl-methacrylate (PMMA) can be spun-casted onto the graphene and then the copper foil etch-removed by floating the sample in $FeNO_3$ solution. After the metal is removed, graphene is transferred to a water bath before subsequent transfer onto the photonic crystal membranes. Acetone can be used to dissolve the PMMA layer, and the sample rinsed with isopropyl alcohol and dry baked for the measurements.

Optical measurements

[0043] Continuous-wave finely-tuned semiconductor lasers from 1520 to 1620 nm (200 kHz bandwidth and -20 dBm to 7 dBm powers) can be used for optical measurements. Lensed tapered fibers (Ozoptics) with polarization controller and integrated on-chip spot size converters can be used. Without the graphene cladding (in the control sample), the total fiber-chip-fiber transmission is ~ -10 dB. The fiber to channel waveguide coupling is optimized to be 3 dB per input/output facet, with 1 to 2 dB loss from channel to photonic crystal waveguide coupling. The linear propagation loss for our air-cladded photonic crystal waveguide is determined at 0.6 dB/mm; for a photonic crystal waveguide length of 0.12 mm, the propagation loss in the waveguide is negligible. The output is monitored by an amplified InGaAs photodetector (Thorlab PDA10CF, DC-150 MHz bandwidth) and oscilloscope (WaveJet 314A, 100 MHz bandwidth, 3.5 ns rise time) for the time-domain oscillations. The four-wave mixing pump laser linewidth is 10 pm (~ 12 GHz). Confocal microscopy is used for the graphene Raman spectroscopic measurements with a 100× (numerical aperture at 0.95) objective, pumped with a 514 nm laser.

Numerical simulations

[0044] The three dimensional finite-difference-time-domain (FDTD) method with sub-pixel averaging is used to calculated the real and imaginary parts of the *E*-field distribution for the cavity resonant mode. The spatial resolution is set at 1/30 of the lattice constant (14 nm). Time-domain coupled mode theory including dynamic free carrier and thermal dispersion is carried out with 1 picosecond temporal resolution.

Dynamic conductivity and optical absorption of graphene

Estimating the Fermi level in CVD grown grapheme

[0045] The Raman spectra are shown in **Figure 1B** and **Figure 5A**. The G and 2D band peaks are excited by the 514 nm green laser and are located at 1582 cm^{-1} and 2698 cm^{-1} respectively. The Raman spectra are homogeneous within one device, and vary less than 5 cm^{-1} from sample to sample. The Lorenzian line-shape with full width half maximun of the G (34.9 cm^{-1}) (**111**) and 2D (49.6 cm^{-1}) (**112**) band indicates the graphene monolayer. The phonon transport properties, represented by the position of the G and 2D peaks, varying within 1 cm^{-1} over the sample, and the intensity ratio between 2D and G peak, fluctuate from 1 to 1.5, indicating single layer and ~ 5×10^{12} cm^{-2} p doping. Good uniformity of graphene is checked by symmetrical single raman G peak **111**. **Figure 5A** depicts Raman G peak (black line **501**) and its reverse (grey dashed line **502**). The inset **503** shows an optical image of a device transferred according to an embodiment of the present subject matter. The 2D peak is observable only when the laser excitation energy (E_L) and the energy corresponding to electron-hole recombination process (E_T) follow the relation: $(E_L-E_T)/2>E_F$, where E_F is the Fermi energy of graphene. With 514 nm laser excitation, the 2D peak is located at 2698 cm^{-1} (**Figure 1B** and **Figure 5A**). Here, $(E_L-E_T)/2 = \pi\hbar\times(2698\ cm^{-1}) = 0.17$ eV, which means the Fermi level is within ± 0.17 eV of the Dirac point.

[0046] **Figure 5B** and **5C** illustrates example transfers of large-area CVD graphene into various substrates including poly(methyl methacrylate) [PMMA] (**513**), air-bridged silicon membranes, silicon oxide, and partially covered metal surfaces (**514**). CVD grown graphene is thicker and has rough surface compared to exfoliated graphene, shown by the broadened 2D peak and the fluctuation of the 2D versus G peak ratio. The thickness of graphene is ~ 1 nm. The wrinkles on the surface are formed during the cooling down process, due to the different expansion coefficient between the copper and graphene, and typically only on the edges of samples, consistently and readily observable in the samples. At the device regions most of the devices are covered with a single unwrinkled graphene layer. **Figure 5B** depicts a centimeter-scale graphene film **511** prepared in accordance with an embodiment of the present subject matter. A dime **512** is included for scale. Optical images **513** and **514** depict graphene film **511** transferred to various substrates (plastics, air-bridged silicon membranes, silicon oxide and partially covered metal surfaces), with the graphene interface pictured. **Figure 5C** depicts a SEM micrograph **520** of an example air-bridged device sample in accordance with an embodiment of the present subject matter. Graphene covers the whole area except the dark (exposed) region **521**. Scale bar **522** is 500 nm.

[0047] Wet transfer of graphene is used in these measurements. While a very thin (in the range of a nanometer) residual layer of PMMA typically remains on the sample after transfer, PMMA typically only has a non-centrosymmetric $\chi^{(2)}$ response with a neglible $\chi^{(3)}$ response and hence does not contribute to the enhanced four-wave mixing observations. The dopants can arise from residual absorbed molecules or ions on graphene or at the grain boundaries, during the water bath and transfer process. With the same CVD growth process, the dry transfer technique which controls the doping density is low enough such that the Fermi level is within the interband optical transition region. In that case, the measured samples have a

significant increased fiber-chip-fiber coupling loss from ~0 dB to +11 dB over the 120 μm length photonic crstal waveguide (~ 0.01 dB/μm) and the resulting absorption and low pump power in the cavity prevents the various nonlinear observations as described herein. **Figure 5D** depicts a Raman spectrum of the graphene-cladded silicon in accordance with an embodiment of the present subject matter.

Calculations of graphene's dynamic conductivity

[0048] Given the fact that CVD graphene is heavily p-doped, the dynamic conductivity for intra- and inter-band optical transitions can be determined from the Kubo formalism according to equations (2) and (3), where e is the electron charge, ħ is the reduced Plank constant, ω is the radian frequency, μ is chemical potential, and τ is the relaxation time (1.2 ps for interband, 10 fs for intraband conductivity). The dynamic conductivity of intra- and inter-band transitions at 1560 nm are $(-0.07-0.90i)\times10^{-5}$ and $(4.15-0.95i)\times10^{-5}$ respectively, leading to the total dynamic conductivity $\sigma_{total}=\sigma_{intra}+\sigma_{inter}$ of $(4.1-1.8i)\times10^{-5}$. Given negative imaginary part of total conductivity, the TE mode is supported in graphene. The light can travel along the graphene sheet with weak damping and thus no significant loss is observed for the quasi-TE mode confined in the cavity.

$$\sigma_{intra}(\omega) = \frac{je^2\mu}{\pi\hbar(\omega+j\tau^{-1})} \qquad (2)$$

$$\sigma_{inter}(\omega) = \frac{je^2\mu}{4\pi\hbar}\ln\left(\frac{2|\mu|-\hbar(\omega+j\tau^{-1})}{2|\mu|+\hbar(\omega+j\tau^{-1})}\right) \qquad (3)$$

[0049] The transferred graphene is electrically isolated from silicon by a 1 nm layer of native silicon oxide and surface roughness. The impurity density of the 250 nm thick silicon membrane is $\sim10^{11}$ cm^{-2} (slightly lower than the doping density in graphene: $\sim5\times10^{12}$ cm^{-2}).

Parameter space of nonlinear optics in graphene nanophotonics

[0050] **Figure 6** depicts a comparison of switching energy versus recovery time of cavity-based modulators and switches across different semiconductor material platforms. The circles **601** are carrier plasma-induced switches with negative detuning, and the squares **602** are thermal-optic switches with positive detuning. The dashed lines **603** illustrate the operating switch energies versus recovery times, for the same material. **Figure 6** compares cavity-based switching and modulation across different platforms including silicon and III-V conventional materials and the hybrid graphene- silicon cavities of the present disclosure. The thermal or free carrier plasma based switching energy is given by $P_{0th/e} \times \tau_{th/e}$, where $P_{0th/e}$ is the threshold laser power required to shift the cavity resonance of half bandwidth through thermal/free carrier dispersion; $\tau_{th/e}$ are the thermal relax/free carrier life lifetime in resonantor. Note that the lifetime should be replace by photon lifetime if the latter one is larger (usully for high Q cavity). Graphene brings about a lower switching energy due to strong two-photon absorption (~3,000 cm/GW). The recovery times of thermal switching (**602**) are also shortened due to higher thermal conductivity in graphene, which is measured for supported graphene monolayers at 600 W/mK and bounded only by the graphene-contact interface and strong interface phonon scattering.

[0051] The switching energy is inversely proportional to two photon absorption rate (β_2). Table 1 summarizes the first-order estimated physical parameters from coupled-mode theory-experimental data matching, from full three-dimensional numerical field simulations, and from directly measured data, further detailed herein. With the enhanced two-photon absorption in graphene and first-order estimates of the reduced carrier lifetimes (detailed below), the switching energy – recovery time performance of the hybrid graphene-silicon cavity is illustrated in **Figure 5**, compared to monolithic GaAs or silicon ones.

Parameter	Symbol	GaAs	Si	Graphene-Si
TPA coefficient	β_2 (cm/GW)	10.2	1.5	25 [3D]
Kerr coefficient	n_2 (m^2/W)	1.6×10^{-17}	0.44×10^{-17}	7.7×10^{-17} [3D]
Thermo-optic coeff.	dn/dT	2.48×10^{-4}	1.86×10^{-4}	
Specific heat	$c_v\rho$ (W/Km^{-3})	1.84×10^{6}	1.63×10^{6} [cal]	
Thermal relaxation time	$\tau_{th,c}$ (ns)	8.4	12	10 [cal]
Thermal resistance	R_{th} (K/mW)	75	25	20 [cal]
FCA cross section	σ ($10^{-22}m^3$)	51.8	14.5	
FCD parameter	ζ ($10^{-28}m^3$)	50	13.4	
Carrier lifetime	τ_{fc} (ps)	8	500	200 [CMT]
Loaded Q	Q	7000	7000 [m]	
Intrinsic Q	Q_0	30,000	23,000 [m]	

Table 1

[0052] Table 1 provides estimated physical parameters from time-dependent coupled-mode theory-experimental matching, three-dimensional numerical field simulations, and measurement data. In the table, [CMT] signifies nonlinear time-dependent coupled mode theory simulation; [3D] signifies three-dimensional numerical field calculation averages; [m] signifies measurement at low power; and [cal] signifies first-order hybrid graphene-silicon media calculations. τ_{fc} is the effective free-carrier lifetime accounting for both recombination and diffusion.

Graphene two-photon absorption and accompanying thermal and free-carrier nonlinearities

[0053] With increasing input power, the transmission spectra evolve from symmetric Lorenzian to asymmetric lineshapes as illustrated in the examples of Figure 1d and Figure 7. Through second-order perturbation theory, the two-photon absorption coefficient β_2 in monolayer graphene is estimated through the second-order interband transition probability rate per unit area according to equation (4), where v_F is the Fermi velocity, $\hbar$ the reduced Planck's constant, e the electron charge, and ε_ω the permitivity of graphene in the given frequency. At 1550 nm wavelengths, β_2 is determined through Z-scan measurements and first-principle calculations to be in the range of ~ 3,000 cm/GW.

$$\beta_2 = \frac{4\pi^2}{\varepsilon_\omega \omega^4 \hbar^3}\left(\frac{vFe^2}{c}\right)^2 \qquad (4)$$

[0054] **Figure 7A** illustrates the *L3* cavity resonance in the transmission spectra with different input powers. **Figure 7A** depicts measured quasi-TE transmission spectra of a graphene-cladded L3 cavity with different input power levels (with extracted insertion loss from the facet of waveguides in order to be comparable to simulation in **Figure 7B**). **Figure 7B** depicts nonlinear coupled mode theory simulated transmission spectra. The estimated input powers are marked in the panels. With thermal effects, the cavity resonance red-shifts 1.2 nm/mW for the graphene-cladded sample (Q ~ 7,000) and only 0.3 nm/mW for silicon sample (similar Q ~ 7,500). These sets of measurements are summarized in **Figure 7C** where the thermal red-shift is sizably larger in the graphene-cladded sample versus a near-identical monolithic silicon cavity. **Figure 7C** depicts measured cavity resonance shifts versus input power, with the graphene-cladded cavity samples according to an embodiment of the present subject matter (**721**) and the monolithic silicon control cavity sample (**722**). In addition, **Figure 7D** shows the tuning efficiency for a range of cavity *Q*s examined herein – with increasing *Q* the monoltihic silicon cavity shows an increase in tuning efficiency while the converse occurs for the graphene-silicon cavity maybe due to the complex coupling between cavity and the waveguide. **Figure 7D** depicts tuning efficiencies for graphene-cladded cavity samples according to an embodiment of the present subject matter (**731**) and control cavity samples (**732**) for a range of cavity loaded *Q*-factors examined.

[0055] The nonlinear cavity transmissions can be modeled with time domain nonlinear coupled mode theory for the dynamics of photon, carrier density and temperature according to equations (5), (6), and (7),where a is the amplitude of resonance mode; N is the free carrier density; ΔT is the cavity temperature shift. P_{in} is the power carried by incident CW laser

wave. κ is the coupling coefficient between waveguide and cavity, adjusted by the backgroud Fabry-Perod resonance in waveguide. ω_L-ω_0 the is detuning between the laser frequency (ω_L) and cold cavity resonance (ω_0). The time dependent cavity resonance shift is $\Delta\omega=\Delta\omega_N-\Delta\omega_T+\Delta\omega_K$, where the free carrier dispersion is $\Delta\omega_N=\omega_0\zeta N/n$; thermal induced dispersion is $\Delta\omega_T=\omega_0\Delta T(dn/dT)/n$. $\Delta\omega_K$ is Kerr dispersion, and is negligibly small compared to the other two.

$$\frac{da}{dt} = \left(i(\omega_L - \omega_0 + \Delta\omega) - \frac{1}{2\tau_t}\right)a + \kappa\sqrt{P_{in}} \qquad (5)$$

$$\frac{dN}{dt} = \frac{1}{2\hbar\omega_0\tau_{TPA}}\frac{V_{TPA}}{V_{FCA}^2}|a|^4 - \frac{N}{\tau_{fc}} \qquad (6)$$

$$\frac{d\Delta T}{dt} = \frac{R_{th}}{\tau_{th}\tau_{FCA}}|a|^2 + \frac{\Delta T}{\tau_{th}} \qquad (7)$$

[0056] The total loss rate is $1/\tau_t = 1/\tau_{in}+1/\tau_v+1/\tau_{lin}+1/\tau_{TPA}+1/\tau_{FCA}$. $1/\tau_{in}$ and $1/\tau_v$ is the loss rates into waveguide and into freespace, ($1/\tau_{in/v} = \omega/Q_{in/v}$), the linear absorption $1/\tau_{lin}$ for silicon and graphene are demonstrated to be small. The free carrier absorption rate $1/\tau_{FCA}=c\sigma N(t)/n$. The field averaged two photon absorption rate $1/\tau_{TPA} = \overline{\beta_2}c^2/n^2/V_{TPA}|a|^2$, where the effective two photon absorption coeffient is defined according to equation (8) (similar to field averaged Kerr coefficient below). The mode volume for two photon absorption if given in equation (9) (same as Kerr). The effective mode volume for FCA is given in equation (10).

$$\overline{\beta_2} = \left(\frac{\lambda_0}{2\pi}\right)^d \frac{\int n^2(r)\beta_2(r)\left(|E(r)\cdot E(r)|^2+2|E(r)\cdot E(r)^*|^2\right)d^dr}{\left(\int n^2(r)|E(r)|^2 d^dr\right)^2} \qquad (8)$$

$$V_{TPA/Kerr} = \frac{\left(\int n^2(r)|A(r)|^2 dr^3\right)^2}{\int_{Si} n^4(r)|A(r)|^4 dr^3} \qquad (9)$$

$$V_{FCA}^2 = \frac{\left(\int n^2(r)|A(r)|^2 dr^3\right)^3}{\int_{Si} n^6(r)|A(r)|^6 dr^3} \qquad (10)$$

[0057] The model shows remarkable match to the measured transmissions. With the two-phtoton absorption and Kerr coefficients of the hybrid cavity calculated from 3D finite-different time-main field averages and first-order estimates of the thermal properties (specific heat, effective thermal resistance and relaxation times), the carrier lifetime of the graphene-cladded photonic crystal cavity is estimated to first-order at 200 ps.

Regenerative oscillations in graphene-cladded silicon cavities

[0058] Regenerative oscillations are observed in silicon microdisks with Q at 3×10^5 and V at $40(\lambda/n_{Si})^3$, at sub-milliwatt power levels. The graphene-enhanced two-photon absorption, free-carrier and thermal effects allow regenerative oscillations to be experimentally observable with Q^2/V values [of $4.3\times10^7(\lambda/n)^3$] at least 50× lower, at the same power threshold levels. The regenerative oscillations with lower Qs allow higher speed and wider bandwidth operation, and are less stringent on the device nanofabrication.

[0059] **Figure 8A** depicts resonance wavelength shift, where the curve **801** and curve **802** represent the free-carrier dispersion and the thermal dispersion, respectively. Curve **803** is the net cavity resonance evolving with time. Dashed lines **804**, **805**, and **806** indicate the resonance shifts in silicon cavity without graphene at the same power level and detuning. Dashed lines **804**, **805**, and **806** are correspondent to free carrier, thermal, and total resonance shift. **Figure 8B** depicts cavity temperature shifts versus free carrier density.

Figure 8A and 8B illustrates the numerical comparison of the time-domain regeneration oscillations, with and without the graphene, on a photonic crystal L3 cavity. As shown in **Figure 8**, the free carrier induced cavity resonance blue-shift is competing with the thermal induced cavity red-shift. **Figure 9** depicts free-carrier absorption effects on the four-wave mixing conversion efficiency. Measured idler power versus signal power at the transmitted port, with the pump power is fixed on the cavity resonance and the signal laser detuned by

200 pm. Experimental data is show as ×s **901** and a quadratic fit is depicted as solid line **902**. Inset **903** corresponding to conversion efficiency versus signal power.

Ultrafast Kerr in graphene – silicon hybrid structures

Computations of effective Kerr nonlinearity in graphene-Si cavity

[0060] Third-order nonlinearity susceptibility for graphene is reported as large as $|\chi^{(3)}|\sim10^{-7}$ esu in the wavelength range of 760 to 840 nm. When two external beam with frequency ω_1 (pump) and ω_2 (signal) incident on graphene, the amplitude of sheet current generated at the harmonics frequencies ($2\omega_1$-ω_2) is given in equation (11), where ε_1, ε_2 are electric field amplitude of the incident light at frequency ω_1 and ω_2 respectively. v_F (=10^6 m/s) is the Fermi velocity of graphene. Under the condition that both ω_1 and ω_2 are close to ω, the sheet conductivity can be approximated according to equation (12). Since most of the sheet current is generated in graphene, the effective nonlinear susceptibility of the whole membrane can be expressed according to equation (13), where d is the thickness of the graphene (~1 nm), λ the wavelength, and c is the speed of light in vacuum. The calculated $\chi^{(3)}$ is in the order of 10^{-7} esu (corresponding to a Kerr coefficient $n_2 \sim 10^{-13}$ m^2/W), at 10^5 times higher than in silicon ($\chi^{(3)}\sim 10^{-13}$ esu, $n_2 \sim 4\times10^{-18}$ m^2/W).

$$j_e = -\frac{3}{32}\frac{e^2}{\hbar}\varepsilon_2\left(\frac{ev_F\varepsilon_1}{\hbar\omega_1\omega_2}\right)^2\frac{2\omega_1^2+2\omega_1\omega_2-\omega_2^2}{\omega_1(2\omega_1-\omega_2)} \qquad (11)$$

$$\sigma^{(3)} = \frac{j_e}{\varepsilon_1\varepsilon_1\varepsilon_2} = -\frac{9}{32}\frac{e^2}{\hbar}\left(\frac{ev_F}{\hbar\omega^2}\right)^2 \qquad (12)$$

$$\chi^{(3)} = \frac{\sigma^{(3)}}{\omega d} = -\frac{9}{32}\frac{e^4v_F^2}{\hbar^3c^5}\frac{\lambda^5}{d} \qquad (13)$$

[0061] Effective n_2 of the whole membrane can be calculated for an inhomogeneous cross section weighted with respect to field distribution. With a baseline model without complex graphene-surface electronic interactions, the effective n_2 can be expressed according to

equiation (14), where *E(r)* is the complex fields in the cavity and n(r) is local refractive index. The local Kerr coefficient $n_2(r)$ is 3.8×10^{-18} m^2/W in silicon membrane and ~10^{-13} m^2/W for graphene, λ_0 is the wavelength in vacuum, and d=3 is the number of dimensions. The complex electric field E(r) is obtained from 3D finite-difference time-domain computations of the optical cavity examined. The resulting field-balanced effective n_2 is calculated to be 7.7×10^{-17} m^2/W ($\chi^{(3)}$~ 10^{-12} esu). Table 2 gives the field-balanced third-order nonlinear parameters.

$$\overline{n_2} = \left(\frac{\lambda_0}{2\pi}\right)^d \frac{\int n^2(r) n_2(r)\left(|E(r)\cdot E(r)|^2+2|E(r)\cdot E(r)^*|^2\right)d^d r}{\left(\int n^2(r)|E(r)|^2 d^d r\right)^2} \qquad (14)$$

Computed parameters	$\overline{n_2}$ (m^2/W)	$\overline{\beta_2}$ (m/W)
without graphene	3.8×10^{-18}	8.0×10^{-12}
with graphene	7.7×10^{-17}	2.5×10^{-11}

Table 2

[0062] Likewise, the effective two-photon absorption coefficient is computed in the same field-balanced approach, with a result of 2.5×10^{-11} m/W. The resulting nonlinear parameter, $\gamma=\omega n_2/cA_{eff}$, is derived to be 800 $W^{-1}m^{-1}$, from an effective mode area of 0.25 μm^2.

Local four-wave mixing in graphene-cladded photonic crystals cavities

[0063] The conversion efficiency of the single cavity $\eta=|\gamma P_p L'|^2 FE_p^4 FE_s^2 FE_c^2$, where FE_p, FE_s, and FE_c are the field enhancement factor of pump, signal and idler respectively. The effective length L' includes the phase mismatch and loss effects. Compared to the original cavity length (~ 1582.6 nm), the effective cavity length is only slightly modified by less than 1 nm. However, the spectral dependent field enhancement factor is the square of the cavity build-up factor $FE^2=P_{cav}/P_{wg}=F_{cav}(U/U_{max})\eta_p^2$, where U/U_{max} is the normalized energy distribution with the Lorenzian lineshape. $\eta_p=0.33$ is the correction term for the spatial

misalignment between the quasi-TE mode and graphene, and the polarization. The field enhancement effect of in cavity is proportional to the photon mode density: $F_{cav}=Q\lambda^3/(8\pi V)$.

[0064] The enhanced two-photon-absorption and induced free-carrier absorption would produce nonlinear loss. To investigate the direct effect of TPA and FCA on the four wave mixing, the conversion efficiency is measured with varying input signal power. Extra 4 dB loss is measured when the input signal power increases from -22 to -10 dBm. The major contribution is considered coming from the nonlinear loss.

[0065] It is understood that the subject matter described herein is not limited to particular embodiments described, as such may, of course, vary. Accordingly, nothing contained in the Abstract or the Summary should be understood as limiting the scope of the disclosure. It is also understood that the terminology used herein is for the purpose of describing particular embodiments only, and is not intended to be limiting. Where a range of values is provided, it is understood that each intervening value between the upper and lower limit of that range and any other stated or intervening value in that stated range, is encompassed within the disclosed subject matter.

[0066] Unless defined otherwise, all technical and scientific terms used herein have the same meaning as commonly understood by one of ordinary skill in the art to which this disclosed subject matter belongs. Although any methods and materials similar or equivalent to those described herein can also be used in the practice or testing of the present disclosed subject matter, this disclosure may specifically mention certain exemplary methods and materials.

[0067] As used herein and in the appended claims, the singular forms “a,” “an,” and “the” include plural referents unless the context clearly dictates otherwise.

[0068] As will be apparent to those of skill in the art upon reading this disclosure, each of the individual embodiments described and illustrated herein has discrete components and

features which may be readily separated from or combined with the features of any of the other several embodiments without departing from the scope or spirit of the present disclosed subject matter. Various modifications can be made in the method and system of the disclosed subject matter without departing from the spirit or scope of the disclosed subject matter. Thus, it is intended that the disclosed subject matter include modifications and variations that are within the scope of the appended claims and their equivalents.

CLAIMS

What is claimed is:

1. A photonic crystal comprising:

a body formed at least from a silicon material, the body having opposing top and bottom surfaces;

a plurality of cavities disposed on the body, at least some of the cavities defining an opening extending through at least one of the top and bottom surfaces; and

a layer of graphene disposed on at least one surface of the body.

2. The photonic crystal of claim 1, wherein the graphene layer is a monolayer.

3. The photonic crystal of claim 1, wherein the graphene layer is a bilayer.

4. The photonic crystal of claim 1, wherein the body is formed from only silicon material.

5. The photonic crystal of claim 1, wherein at least some cavities define an opening extending through both the top and bottom surfaces of the body.

6. The photonic crystal of claim 1, wherein all of the cavities define an opening through both the top and bottom surfaces of the body.

7. The photonic crystal of claim 1, wherein the plurality of cavities have a shape defined by a wall of the body.

8. The photonic crystal of claim 7, wherein the shape is circular.

9. The photonic crystal of claim 7, wherein a first portion of the wall defining the cavity shape is silicon and a second portion of the wall is graphene.

10. The photonic crystal of claim 9, wherein the first portion of the wall defines a bottom layer and the second portion of the wall defines a top layer.

11. The photonic crystal of claim 1, wherein the plurality of cavities is arranged in a pattern comprising one or more discontinuities.

12. The photonic crystal of claim 9, wherein the pattern is a hexagonal pattern.

13. The photonic crystal of claim 1, wherein the plurality of cavities has a lattice constant of about 420 nm.

14. The photonic crystal of claim 1, wherein at least some of the cavities define an opening having a radius between about 122 nm and about 126 nm.

15. The photonic crystal of claim 1,wherein body has a thickness of about 250 nm.

16. The photonic crystal of claim 1, wherein the top surface and bottom surface are substantially parallel.

17. The photonic crystal of claim 1, wherein the graphene layer is optically transparent to infrared.

18. The photonic crystal of claim 1, wherein the layer of graphene has a thickness of about 1 nanometer.

19. A photonic crystal comprising:

a silicon body having opposing top and bottom surfaces;

a layer of graphene disposed on the body; and

a plurality of cavities defining openings disposed through the top and bottom surfaces of the silicon body.

20. The photonic crystal of claim 19, wherein the plurality of cavities extend through the graphene layer.

21. The photonic crystal of claim 19, wherein the layer of graphene has a thickness of about 1 nanometer.

22. The photonic crystal of claim 19, wherein the graphene layer is transparent to infrared.

23. The photonic crystal of claim 19, wherein the silicon body has a thickness of about 250 nm.

24. The photonic crystal of claim 19, wherein at least some of the cavities define an opening having a radius between about 122 nm and about 126 nm.

25. The photonic crystal of claim 19, wherein the plurality of cavities define a hexagonal pattern.

26. The photonic crystal of claim 19, wherein the plurality of cavities has a lattice constant of about 420 nm

27. A method of fabricating a photonic crystal, said method comprising:

providing a metal foil;

removing a top oxide layer of the metal foil by exposure to a gaseous atmosphere;

depositing carbon on the metal foil to form a graphene layer;

cooling the graphene layer;

coating the graphene layer with poly(methyl methacrylate);

removing the graphene layer from the metal foil;

transferring said graphene layer onto a substrate; and

removing the Poly(methyl methacrylate) coating.

28. The method of claim 27, wherein the Poly(methyl methacrylate) coating is removed by exposure to acetone.

29. The method of claim 27, wherein the graphene is p-doped.

30. The method of claim 27, further comprising etching a plurality of cavities in the silicon body by deep-ultraviolet lithography.

31. The method of claim 27, wherein the gaseous atmosphere is hydrogen and further wherein the method includes exposure to 2 sccm hydrogen gas at 50 mTorr at 1000°C for about 15 minutes.

32. The method of claim 27, wherein the metal foil is copper foil, and further wherein the graphene layer is removed from the foil by application of a $FeNO_3$ solution.

Figure 1A

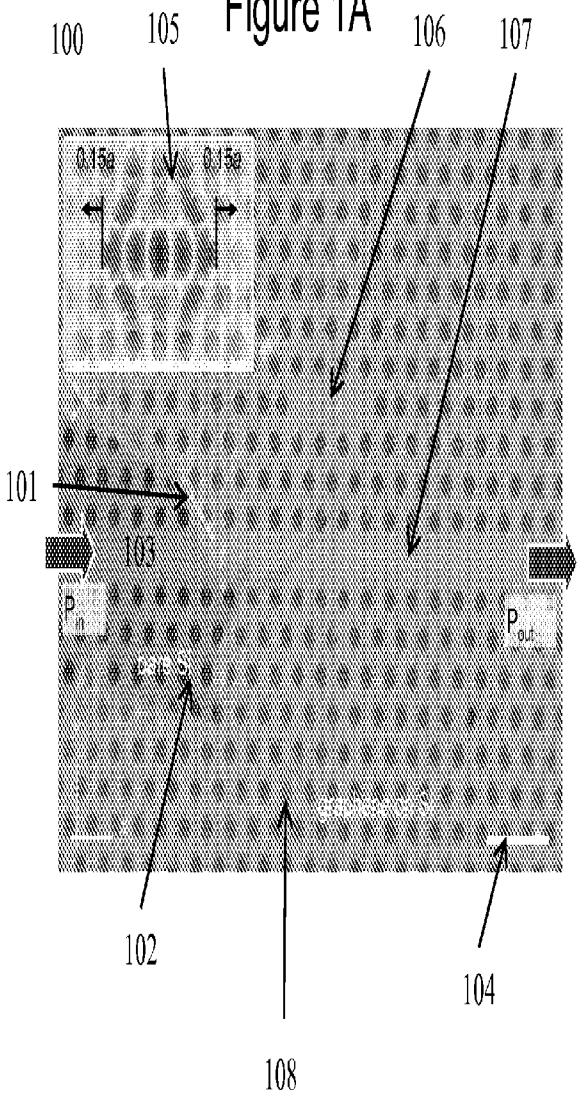

Figure 1B

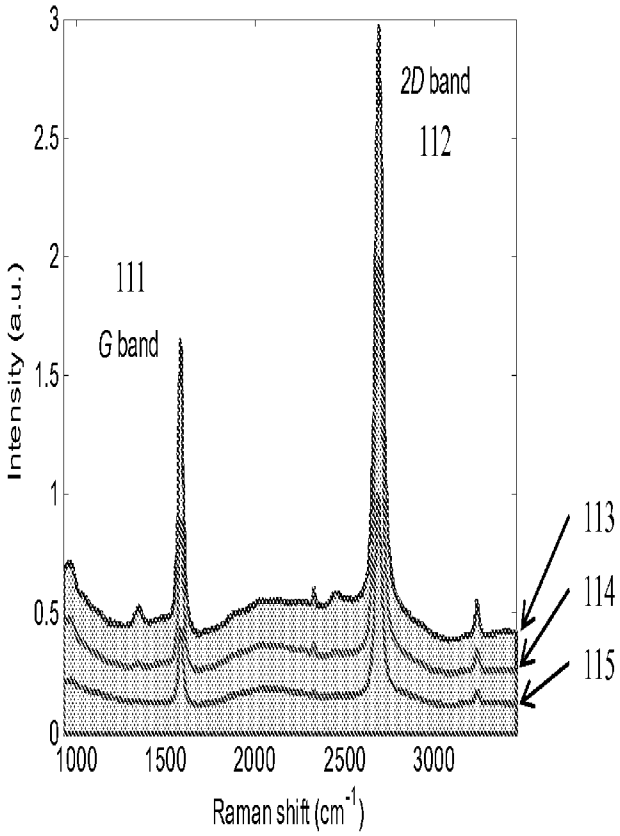

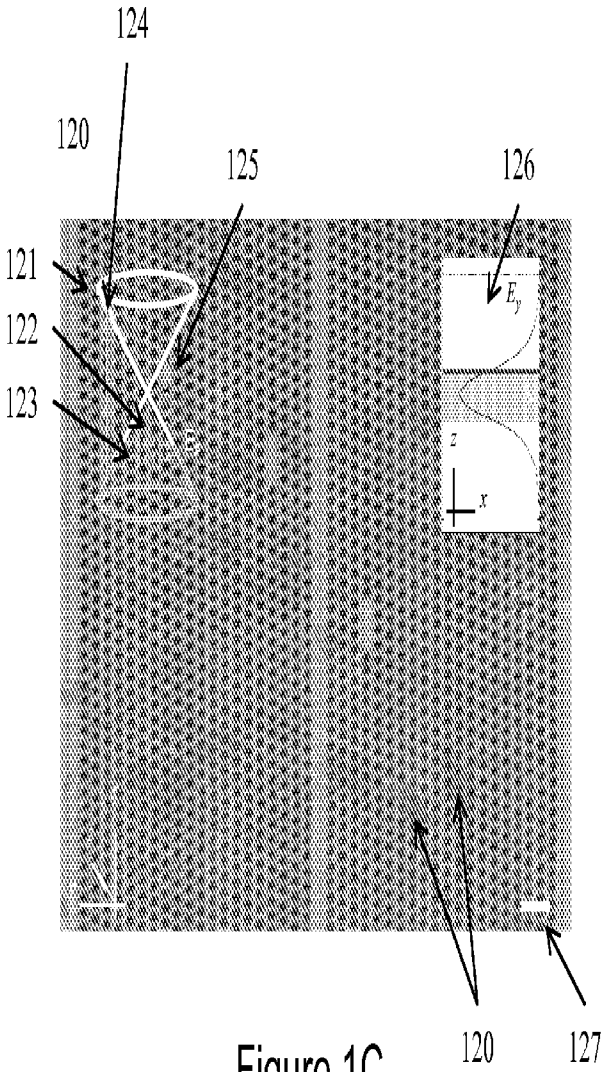

Figure 1C

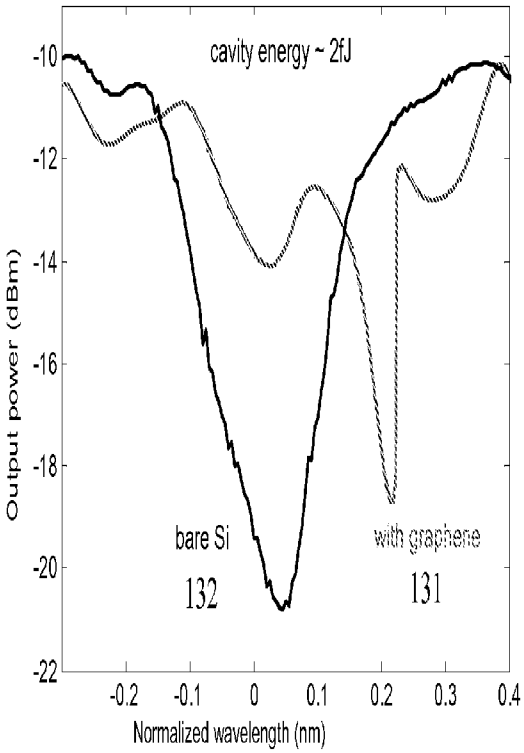

Figure 1D

Figure 2A

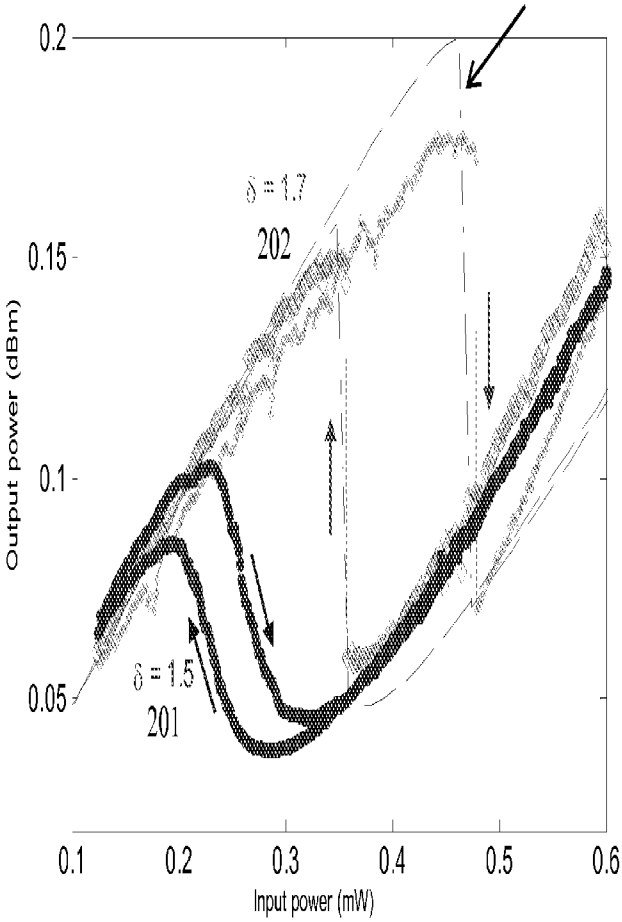

Figure 2B

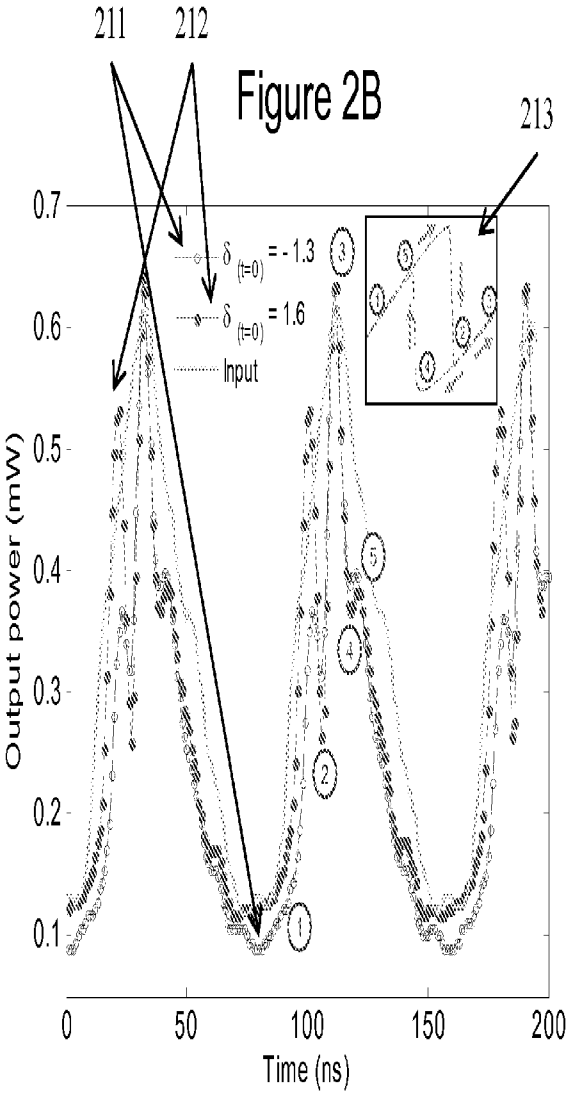

Figure 3A

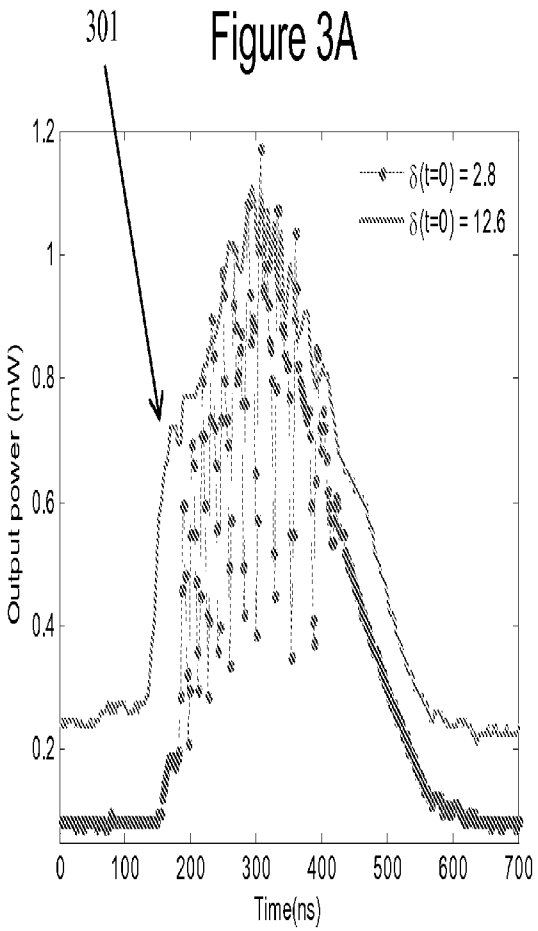

Figure 3B

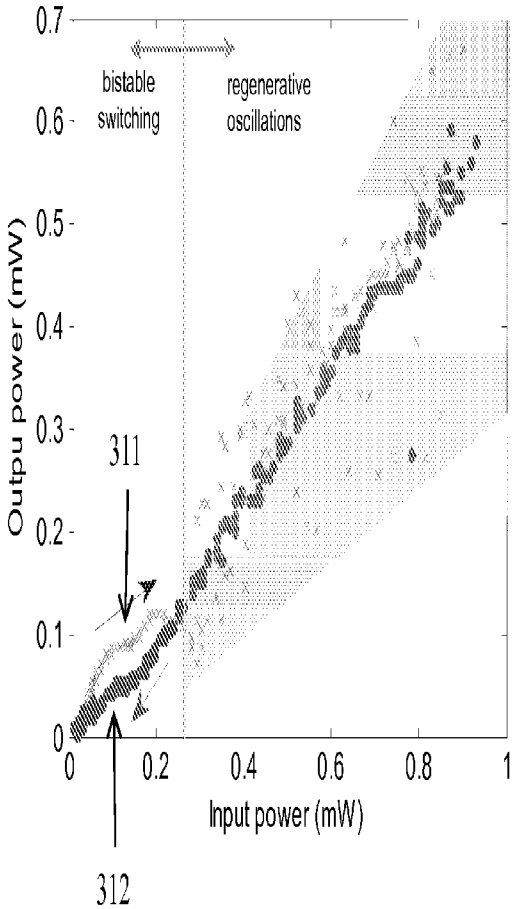

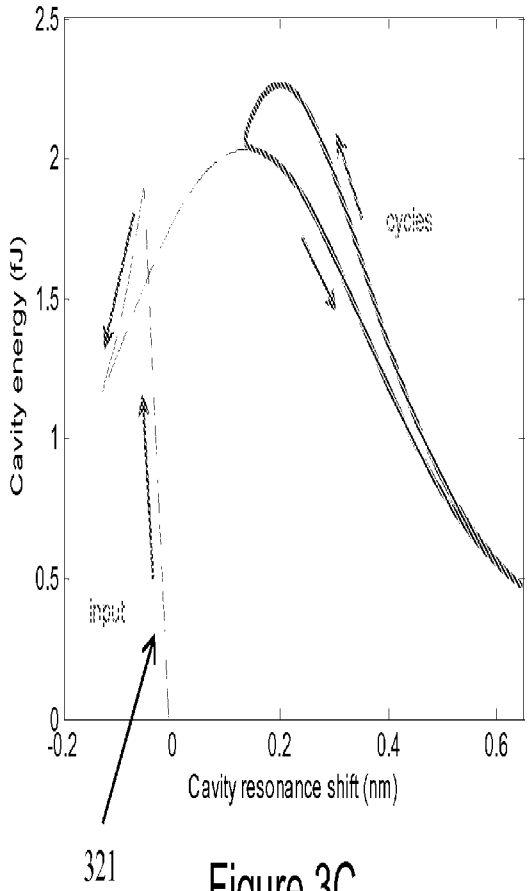

321

Figure 3C

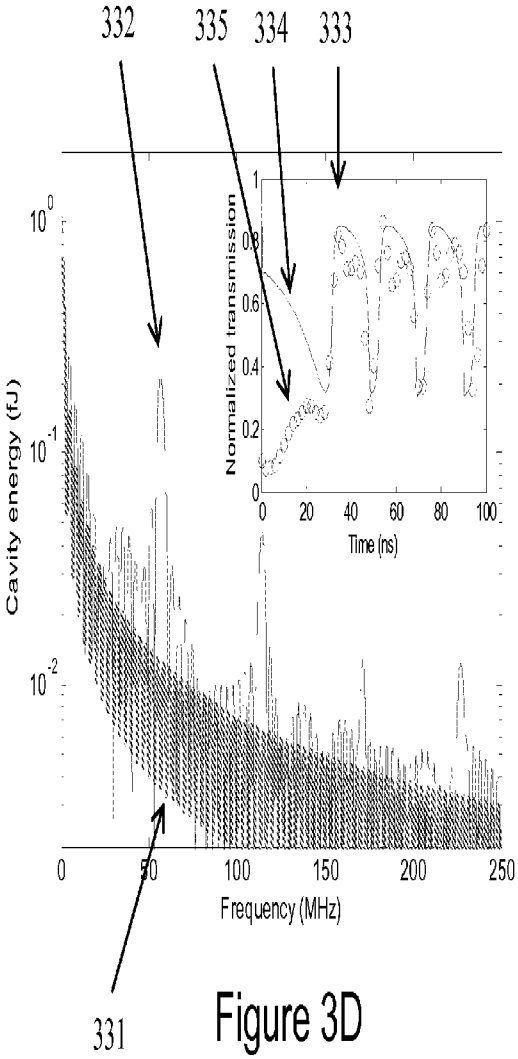

331

Figure 3D

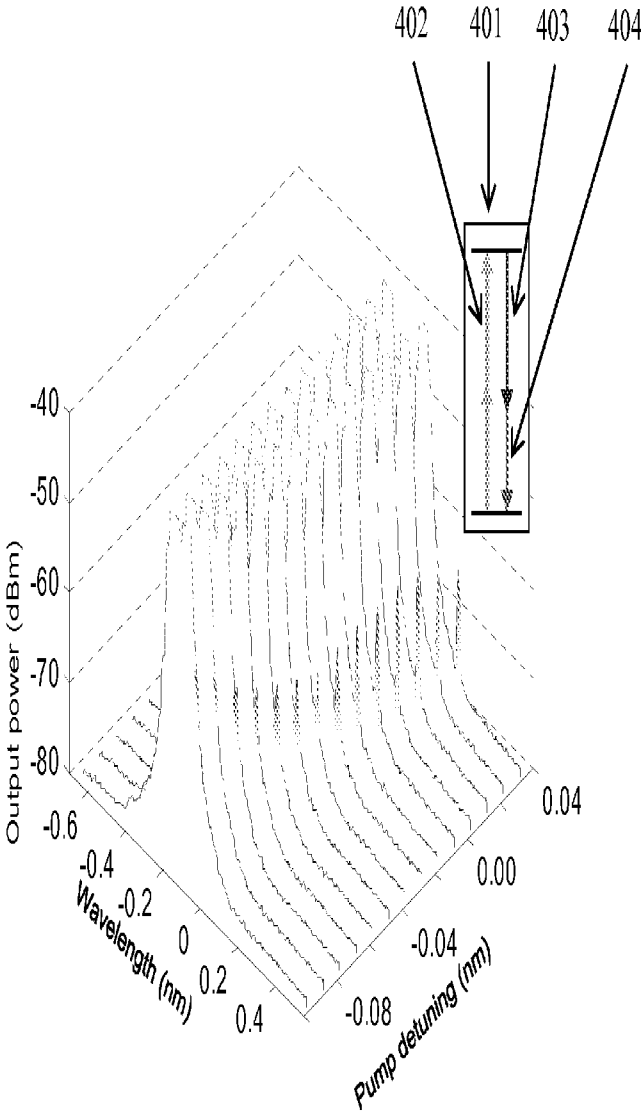

Figure 4A

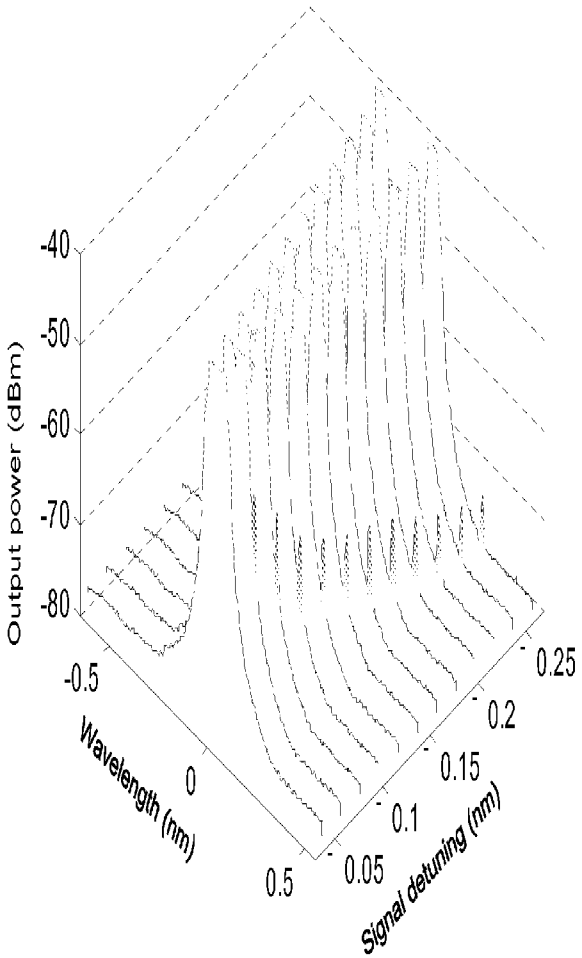

Figure 4B

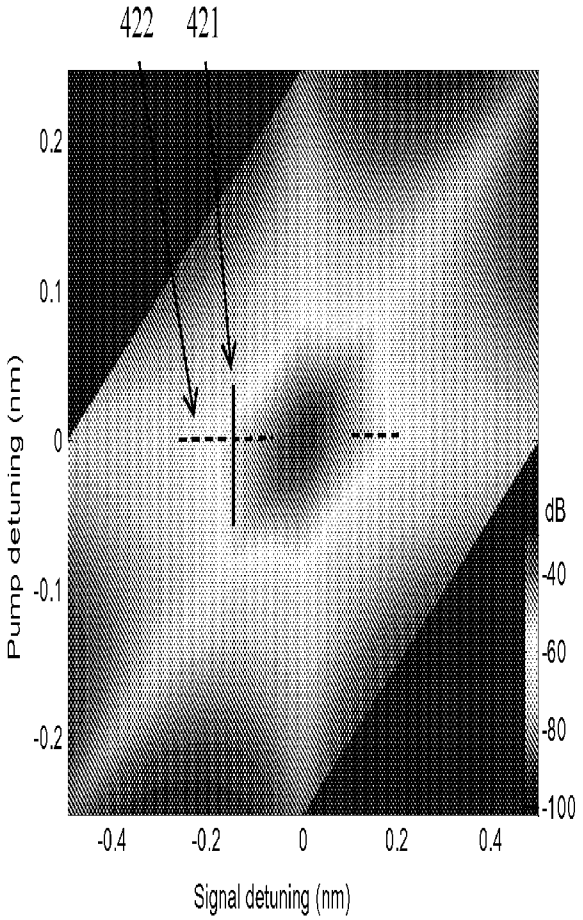

Figure 4C

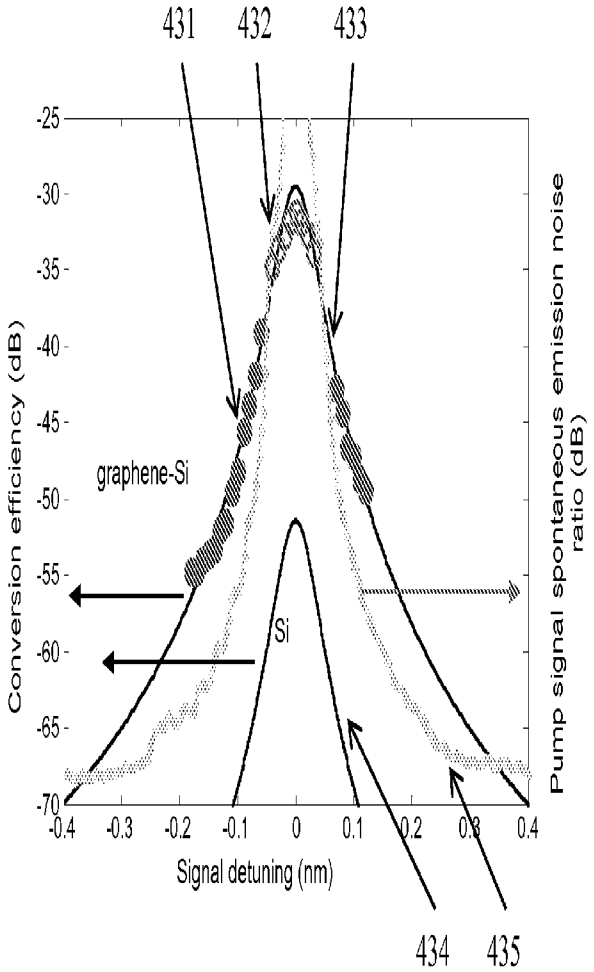

Figure 4D

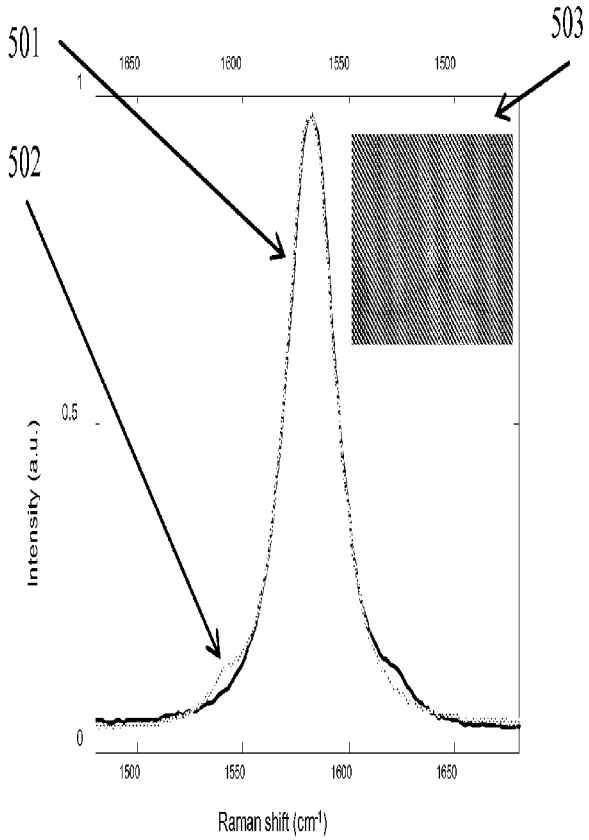

Figure 5A

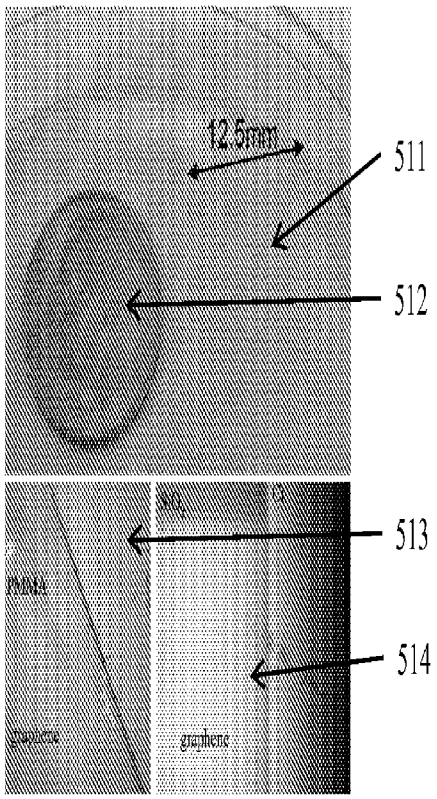

Figure 5B

520

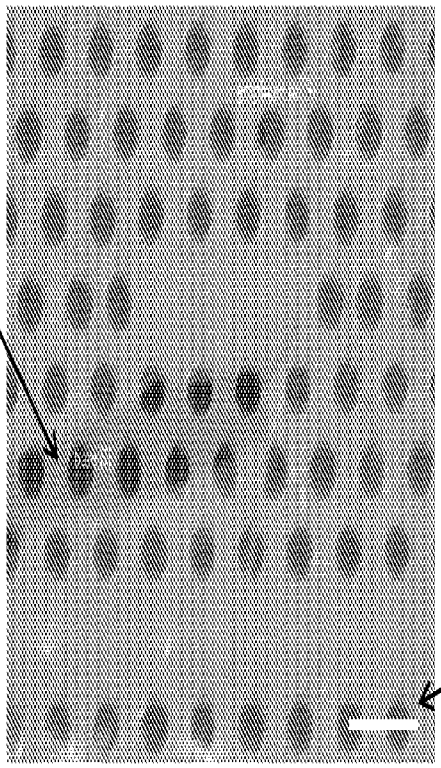

Figure 5C

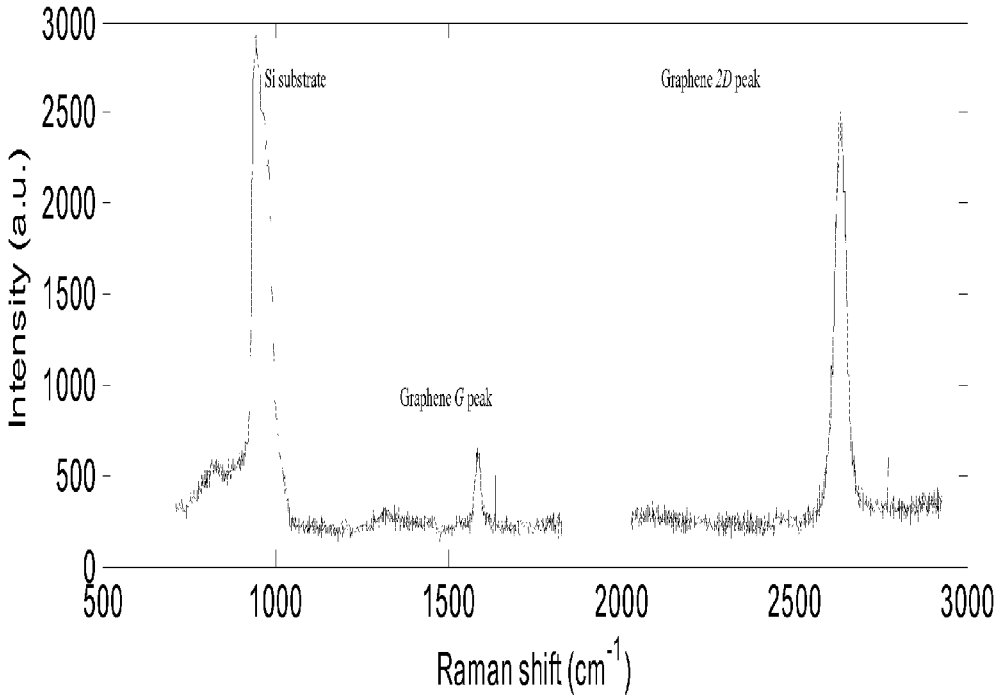
3000
2500
2000
1500
1000
500
0
Intensity (a.u.)
Si substrate
Graphene G peak
Graphene 2D peak
500
1000
1500
2000
2500
3000
Raman shift (cm-1)

Figure 5D

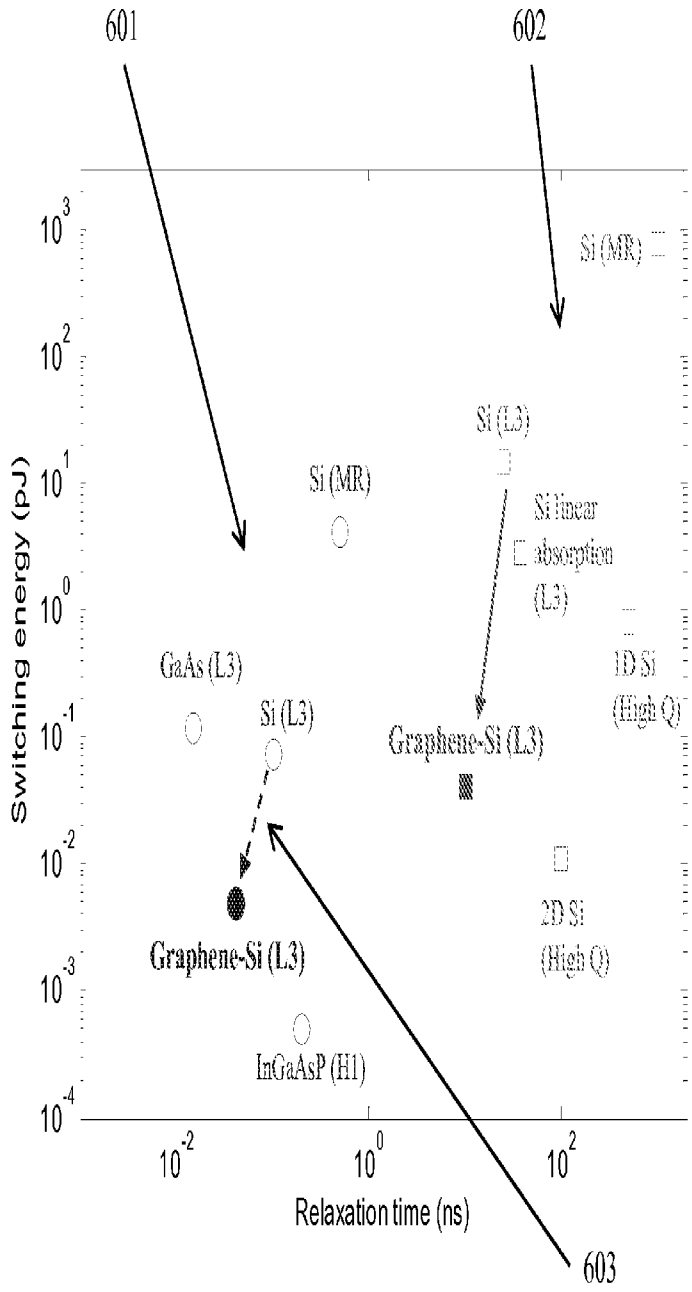
601
602
Si (MR)
Si (L3)
Si (MR)
Si linear absorption (L3)
GaAs (L3)
Si (L3)
Graphene-Si (L3)
1D Si (High Q)
2D Si (High Q)
Graphene-Si (L3)
InGaAsP (H1)
Switching energy (pJ)
Relaxation time (ns)
603

Figure 6

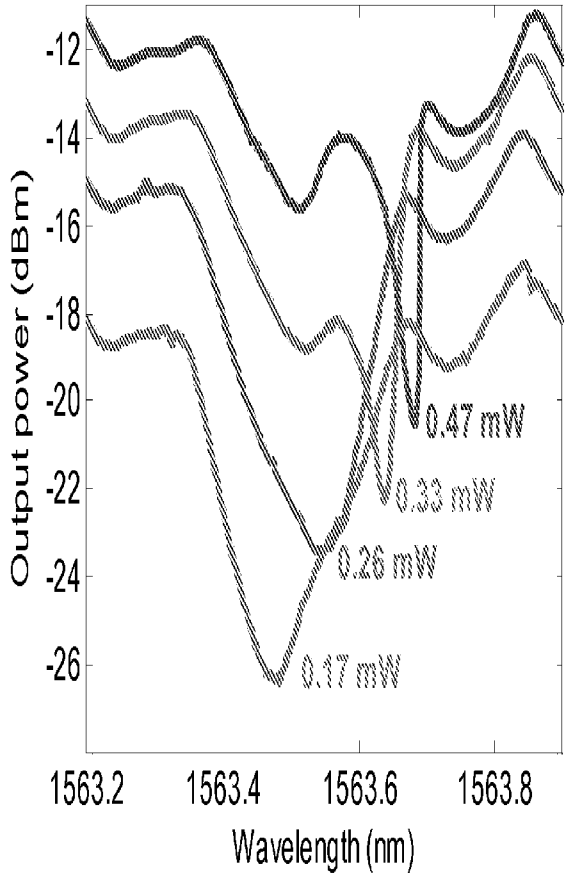

Figure 7A

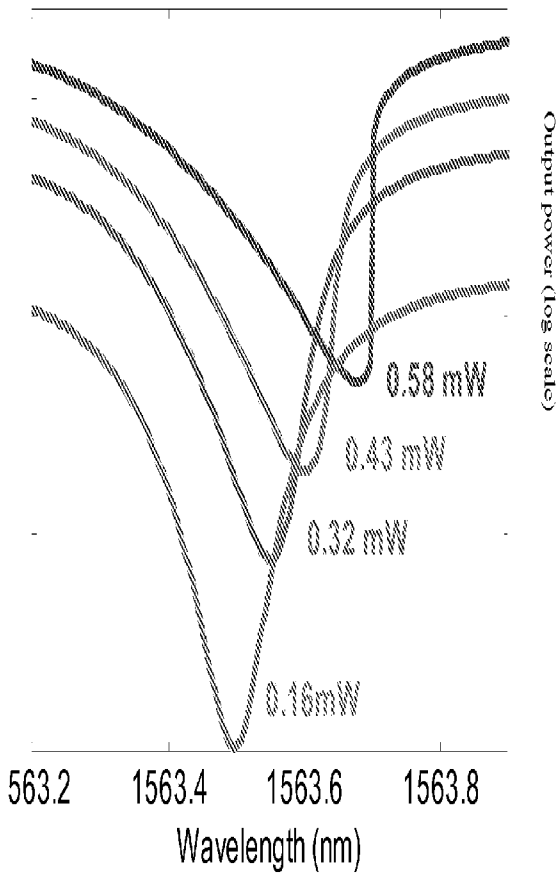

Figure 7B

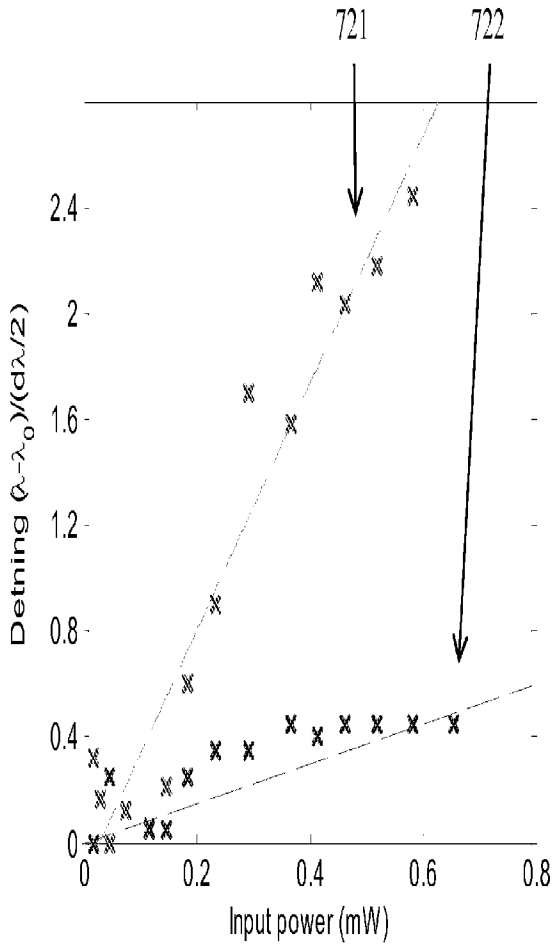

Figure 7C

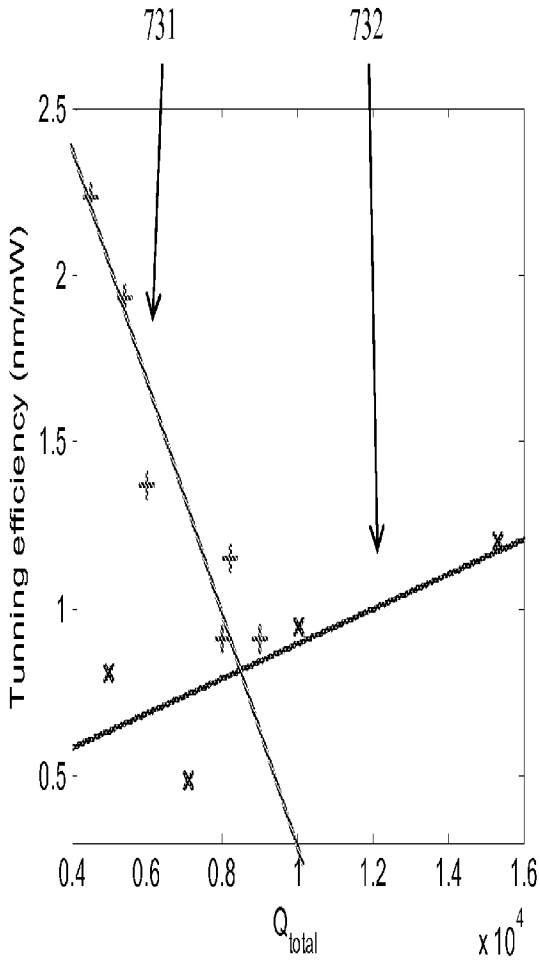

Figure 7D

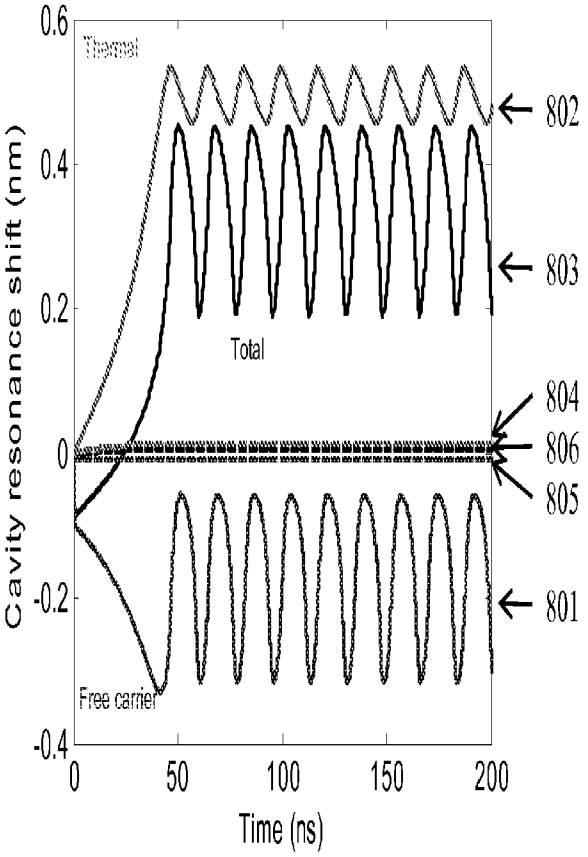

Figure 8A

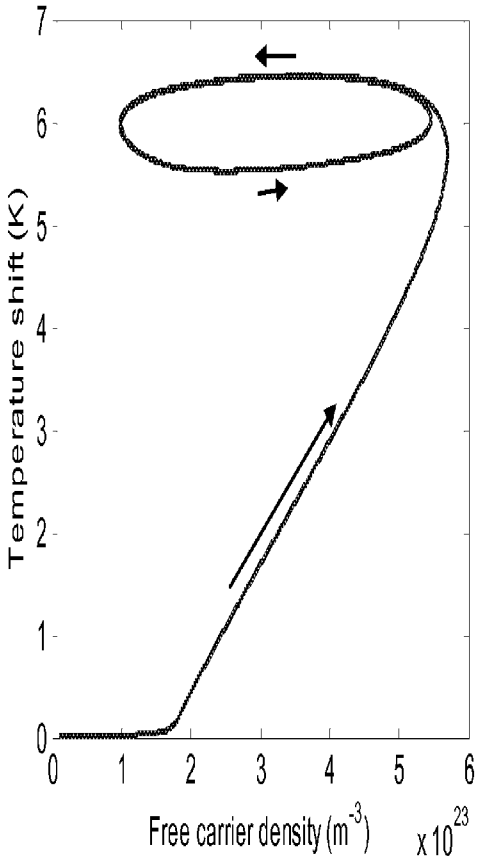

Figure 8B

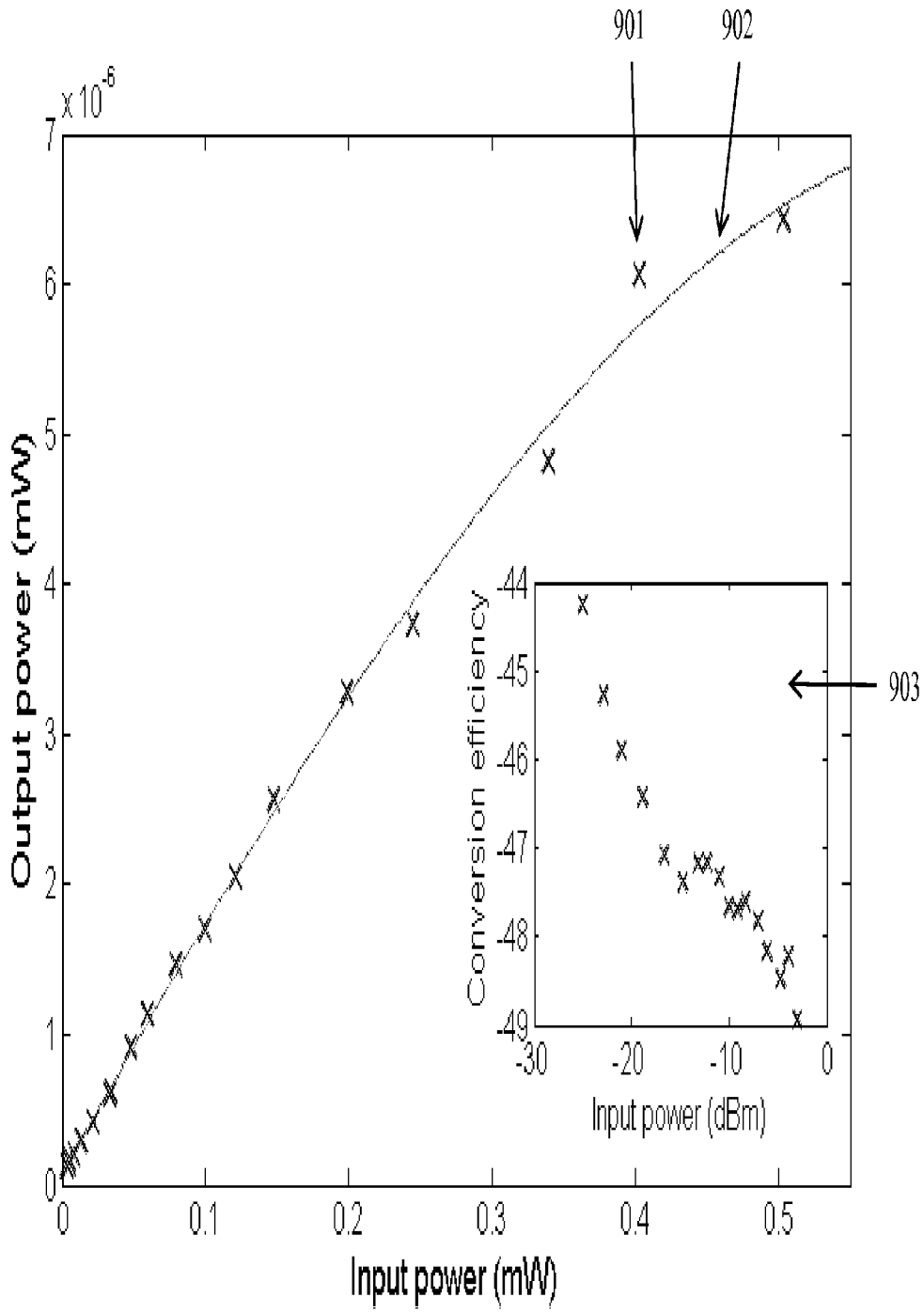
901
902
903
x 10^-6
Output power (mW)
Input power (mW)
Conversion efficiency
Input power (dBm)
0
1
2
3
4
5
6
7
0
0.1
0.2
0.3
0.4
0.5
-44
-45
-46
-47
-48
-49
-30
-20
-10
0

Figure 9

INTERNATIONAL SEARCH REPORT

International application No.
PCT/US2013/020841

A. CLASSIFICATION OF SUBJECT MATTER
IPC(8) - H01L 21/20 (2013.01)
USPC - 257/40
According to International Patent Classification (IPC) or to both national classification and IPC

B. FIELDS SEARCHED

Minimum documentation searched (classification system followed by classification symbols)
IPC(8) - B82B 3/00; B82Y 20/00, 30/00, 40/00; C01B 31/02, 31/04; G02B 6/00; H01L 21/20 (2013.01)
USPC - 216/2; 257/40; 977/742, 773, 842, 932

Documentation searched other than minimum documentation to the extent that such documents are included in the fields searched
CPC - C01B 31/0438, 31/0446; H01L 21/04, 21/2018 (2013.01)

Electronic data base consulted during the international search (name of data base and, where practicable, search terms used)
PatBase, Google Patents, Google Scholar

C. DOCUMENTS CONSIDERED TO BE RELEVANT

Category*	Citation of document, with indication, where appropriate, of the relevant passages	Relevant to claim No.
Y	US 2005/0213868 A1 (CUNNINGHAM) 29 September 2005 (29.09.2005) entire document	1-26
Y	WO 2010/065518 A1 (BOLOTIN et al) 10 June 2010 (10.06.2010) entire document	1-32
Y	US 2011/0017390 A1 (BLAKE et al) 27 January 2011 (27.01.2011) entire document	27-32
Y	US 2011/0147344 A1 (WONG et al) 23 June 2011 (23.06.2011) entire document	13-15, 23, 24, 26
Y	US 7,976,950 B2 (OKAI et al) 12 July 2011 (12.07.2011) entire document	17, 18, 21, 22
Y	US 2009/0047207 A1 (MUHLER et al) 19 February 2009 (19.02.2009) entire document	29, 31, 32

☐ Further documents are listed in the continuation of Box C. ☐

* Special categories of cited documents:
"A" document defining the general state of the art which is not considered to be of particular relevance
"E" earlier application or patent but published on or after the international filing date
"L" document which may throw doubts on priority claim(s) or which is cited to establish the publication date of another citation or other special reason (as specified)
"O" document referring to an oral disclosure, use, exhibition or other means
"P" document published prior to the international filing date but later than the priority date claimed
"T" later document published after the international filing date or priority date and not in conflict with the application but cited to understand the principle or theory underlying the invention
"X" document of particular relevance; the claimed invention cannot be considered novel or cannot be considered to involve an inventive step when the document is taken alone
"Y" document of particular relevance; the claimed invention cannot be considered to involve an inventive step when the document is combined with one or more other such documents, such combination being obvious to a person skilled in the art
"&" document member of the same patent family

Date of the actual completion of the international search	Date of mailing of the international search report
04 March 2013	13 MAR 2013
Name and mailing address of the ISA/US Mail Stop PCT, Attn: ISA/US, Commissioner for Patents P.O. Box 1450, Alexandria, Virginia 22313-1450 Facsimile No. 571-273-3201	Authorized officer: Blaine R. Copenheaver PCT Helpdesk: 571-272-4300 PCT OSP: 571-272-7774

Form PCT/ISA/210 (second sheet) (July 2009)